

**DETECTION OF GADOLINIUM IN LIVER AND KIDNEY
PHANTOMS USING X-RAY FLUORESCENCE**

**DETECTION OF GADOLINIUM IN
LIVER AND KIDNEY PHANTOMS
USING X-RAY FLUORESCENCE**

By MÉLODIE N. CYR, B.Sc.

A Thesis Submitted to the School of Graduate Studies in
Partial Fulfillment of the Requirements for the Degree Master
of Medical Physics

McMaster University © Copyright by Mélodie N. Cyr, 2020

McMaster University MASTER OF SCIENCE (2020) (Radiation Sciences -
Medical Physics) Hamilton, Ontario, Canada

TITLE: Detection of Gadolinium in Liver and Kidney Phantoms using
X-Ray Fluorescence

AUTHOR: Mélodie N. Cyr, B.Sc. (Laurentian University)

SUPERVISORS: Dr. David Chettle, Dr. Fiona McNeill

NUMBER OF PAGES: 1-95

Abstract

Gadolinium (Gd) is commonly used in contrast agents (GBCAs) to improve magnetic resonance imaging. GBCAs improve tumor imaging and were thought to be stable and clear from the body through excretion after administration. However, they have been found to dissociate and remain in organs such as the liver and kidneys. In these studies, a non-invasive Cd-109 based K x-ray fluorescence (K-XRF) “Clover-Leaf” detection system to study liver and kidney Gd levels was investigated to improve the minimum detection limit (MDL). Two Cd-109 sources, one with a relatively low activity of 0.78 GBq and a second high activity source of 5 GBq irradiated a human torso water phantom containing liver and kidney phantoms with Gd concentrations ranging from 0-100 ppm. The MDL was calculated from two different time measurements 5 hours (weak source) and 30 minutes (strong source). In addition, liver and kidney phantom measurements with overlaying tissue thicknesses from 6-26 mm were investigated. At present, the K-XRF detection system is able to detect the Gd in each phantom with both sources. The MDL for the liver and kidney with the weaker source is 2.95 ppm and

3.60 ppm, respectively. The MDL for the stronger source is 3.61 ppm and 3.87 ppm, respectively. The overlaying tissue thickness MDLs decreased exponentially since the thickness increased which increases the scattering and attenuation. Simulations with MCNP successfully modelled the experiments. MCNP simulations of the kidney with varying Gd concentrations in the cortex and medulla suggest that the XRF measurement is not sensitive to the Gd distribution in the phantom. To conclude, this detection system can measure Gd in liver and kidney phantoms and has low MDLs. Future work should focus on varying the detection capabilities, measuring the effects to the organs at risk, possible clinical trials, and improving the MCNP model and peak extraction.

Acknowledgements

The first year at McMaster was definitely difficult and took a lot of work but I ended up overcoming those difficulties and had a fantastic journey. I have become a better researcher and a better person. Thank you to Dr. David Chettle and Dr. Fiona McNeill for being my co-supervisors, providing me with their guidance and excellent knowledge; to Dr. Michael Noseworthy for being on my committee; to all of my colleagues that have helped me with the coding obstacles and other research problems I had to overcome; to my new puppy that reminded me to take breaks and give him lots of attention. I'd also like to thank my friends and family for their constant support during my thesis research and writing process.

Contents

Abstract	ii
Acknowledgements	iv
1 Introduction	2
1.0.1 Gadolinium	3
1.0.2 Nephrogenic Systemic Fibrosis	5
1.0.3 Gadolinium Measurements in Humans	7
1.0.4 X-Ray Fluorescence	8
1.0.5 Detection System	10
1.0.6 Excitation Source	14
1.0.7 Detection of Gadolinium using XRF	15
2 Methods	17
2.0.1 Liver Phantoms	17
2.0.2 Kidney Phantoms	19
2.0.3 Torso Phantom	20

2.0.4	Overlaying Tissue Thickness	22
2.0.5	The Source	22
2.0.6	The Cloverleaf HPGe Detection System	24
2.0.7	Minimum Detection Limit	27
3	Results	31
3.0.1	Liver Phantoms	31
3.0.2	Overlaying Tissue Thickness Liver Phantoms	34
3.0.3	Kidney Phantoms	37
3.0.4	Overlaying Tissue Thickness Kidney Phantom	39
4	Results - New Source Experiments	42
4.0.1	Source-Detector Distance	43
4.0.2	Liver Phantoms	46
4.0.3	Overlaying Tissue Thickness Liver Phantoms	49
4.0.4	Kidney Phantoms	51
4.0.5	Overlaying Tissue Thickness Kidney Phantoms	54
4.0.6	Comparing Live Time with Real Time	56
5	Discussion	58
5.0.1	Comparing MDLs Between the Liver and Kidney	61
5.0.2	Comparing Gd Levels with Other Research	62
5.0.3	Dead Time Configuration	63
5.0.4	Comparison of Neutron Activation Analysis vs. K-XRF	64

5.0.5	High Activity Source	66
5.0.6	Comparing Liver vs. Kidney	67
5.0.7	Comparing the Two Sources	67
6	MCNP Simulations	69
7	MCNP Results & Discussion	73
7.0.1	Kidney Simulations	73
7.0.2	Liver Simulations	76
7.0.3	Cortical Kidney Simulations	79
8	Conclusion	83
8.0.1	Moving Forward	84
8.0.2	Clinical Studies	85
8.0.3	Detector Capabilities	85
8.0.4	MCNP Simulations	88
8.0.5	Conclusions	89

List of Figures

1.1	Depletion region for a germanium semiconductor crystal. Also called a p-n junction between the two p-type and n-type semiconductor materials. The charge carriers are pulled away from the depletion region when a negative bias is applied.	12
1.2	Planar detection configuration with a larger depletion region specific to a HPGe detector.	13
1.3	Decay scheme of Cd-109.	15

1.4 This is an example of an atom with varying electron shells.
 The K shell series is observed with the red and is associated
 in the case of the two characteristic x-rays for Gd. The $K\alpha_1$
 x-ray of energy 42.996 keV is the resultant from the transition
 of an electron moving from L_3 shell to the K shell. As for $K\alpha_2$,
 of energy 42.308 keV, is the resultant x-ray from an electron
 transitioning from the L_2 shell to the K shell [14]. There are
 also $K\beta$ x-rays emitted but since they are higher in energy
 than the $K\alpha$ series and buried in the Compton continuum,
 they are not useful for this analysis. 16

2.1 100 μg Gd/g liver phantom bottle. 19

2.2 Human torso phantom with the liver phantom lowered into
 the cavity, making it the ideal experimental set-up. 21

2.3 The measurement geometry is near backscatter, the source-
 detector to the front of the liver or kidney phantom is the
 only distance that needs to be varied. The source-detector to
 front of torso phantom can stay constant. 23

2.4 Cd-109 source placed inside its capsule, with a copper face,
 then placed in the plastic holder in front of the face of the
 detectors. 24

2.5 Detector face with the plastic holder. Inside there are the four
 HPGe detectors in a “cloverleaf” formation. 25

2.6 Double Gaussian peak fitting to the two Gd $K\alpha_2$ at 42.308 keV and $K\alpha_1$ peaks at 42.996 keV, with a fourth-order polynomial background fit. The blue dots are the data points from energy spectrum of detector 4. This is the experimental measurement of the kidney phantom at 100 μg Gd/g phantom, and the red line is the fit. 26

2.7 Kidney phantom calibration line where the peak area is plotted against the phantom concentrations of Gd. A linear regression analysis fit the data points. The intercept is negative since the peak areas are subtracted by the background. The Gd concentration does have an error, but the error bars are not visible since they are small. The Gd concentration error stems from the pipette (P1000), pipette (P200), as well as from a graduated cylinder. 28

3.1 Calibration line for the four combined detectors. The measured Gd peak area as a function of the known Gd phantom concentrations for the liver phantoms. It was measured at 6 ± 0.5 mm from the Cd-109 source for a duration of 5 hours. The black is the combined $K\alpha_1$ and $K\alpha_2$ peak areas with error bars, fit with a red linear regression. The error bars are small and not easily seen, they reflect only the counting statistics. This line has an R-squared value of 0.98. 33

3.2 Peak area plotted as a function of the overlaying tissue thickness for the MDL calculation. It was fit was a linear regression analysis, in red. The black is the combined Gd $K\alpha_1$ and $K\alpha_2$ with error bars. This is the plot for all four combined detectors. 35

3.3 Natural logarithmic MDL as a function of tissue thickness for the liver phantoms. The values are the combined Gd peaks $K\alpha_1$ and $K\alpha_2$, where the original MDL is in black and the MDL with the time and activity adjustments is in red. These are the data from all four combined detectors. 36

3.4 Calibration line for the four combined detectors. The measured Gd peak area as a function of the known Gd phantom concentrations for the kidney phantoms. It was measured at 6 ± 0.5 mm from the Cd-109 source for the duration of 5 hours. The black is the combined $K\alpha_1$ and $K\alpha_2$ peak areas with error bars, fit with a red linear regression. This line has an R-squared value of 0.98. 38

3.5 Peak area plotted as a function of the overlaying tissue thickness for the MDL calculation. It was fit with an exponential analysis, in red. The black is the combined Gd $K\alpha_1$ and $K\alpha_2$ with error bars. This is the plot for the four combined detectors. 40

3.6 The MDL plotted as a function of overlaying tissue thickness. The black is the original MDL and the red is the adjusted MDL. This is for the four combined detectors. 41

4.1 Detector 3 peak areas as a function of distance. The error bars are included. The peak areas were small once the distance was past 20 mm but the dead time was reasonable. The peak analysis fit was getting distorted for the distance of 5 mm, therefore the 10 ± 0.5 mm distance for the water torso phantom from the source was chosen. For this distance, the peak area was still high while the peak area analysis fit was not yet distorted. The detectors were not saturated although the dead time was quite large. 44

4.2 GBCA available in the laboratory. Omniscan (gadodiamide) in a 20 ml bottle. This bottle was inserted into a plastic bag and then into the water torso phantom for experimental measurements to help determine the source-to-detector distance. 45

4.3 Calibration line for the four combined detectors. The peak area as a function of Gd concentration for the liver phantoms. It was measured at 11 ± 0.5 mm from the source for a duration of 30 minutes. The black is combined $K\alpha_1$ and $K\alpha_2$ peak areas with error bars, fit with the red linear regression. This line has an R-squared value of 0.99. 48

4.4 Peak area as a function of the overlaying tissue thickness for the MDL calculation. It was fit with a linear regression analysis in red and the black is the combined Gd $K\alpha_1$ and $K\alpha_2$ with error bars. This is the plot for the four combined detectors. 50

4.5 Natural logarithmic MDL as a function of tissue thickness for the liver phantoms. The black is the combined Gd peaks $K\alpha_1$ and $K\alpha_2$, it is the original MDL with no adjustments. These are the data from the four combined detectors. 51

4.6 Calibration line for the four combined detectors. The measured Gd peak area as a function of the known Gd phantom concentrations for the kidney phantoms. It was measured at 11 ± 0.5 mm from the Cd-109 source for a duration of 30 minutes. The black is the combined $K\alpha_1$ and $K\alpha_2$ peak areas with error bars, fit with a red linear regression. This line has an R-squared value of 0.99. 53

4.7 Peak area as a function of the overlaying tissue thickness for the MDL calculation. The black is the combined $K\alpha_1$ and $K\alpha_2$ Gd peaks, with error bars, fit with a red exponential fit. This is the plot for the four combined detectors. 55

4.8 The natural logarithmic MDL plotted as a function of the overlaying tissue thickness. The black is the original MDL. This is the MDL plot for the four combined detectors. 56

6.1	MCNP geometry of the detection system with the cortical kidney phantom inside the torso phantom.	72
7.1	Calibration line for the four combined detectors. Where the peak area per emitted source photon is plotted as a function of the Gd concentration for the MCNP simulated data. The black is the combined $K\alpha_1$ and $K\alpha_2$ Gd peaks fitted with the red linear regression.	74
7.2	Normalization plot for the four combined detectors, comparing the experimental and simulated data. The grey line is the simulated data fit with a linear regression. The red is the experimental results fit with a linear regression. The intercept is at 0 since the data is normalized to 1 at the 100 ppm phantom.	75
7.3	Simulated data for the four combined detectors, showing the peak area as a function of Gd concentration. The black is the combined Gd $K\alpha_1$ and $K\alpha_2$ peak areas and the red is the linear fit. The intercept is negative due to the background being subtracted from the peak areas.	77
7.4	Normalization data for the four combined detectors, where the peak area for the simulation and the experiment are plotted as a function of the Gd concentration. The grey are the simulated normalized data with a linear fit. The red are the experimental normalized data fit with a red linear regression.	78

7.5 Peak area as a function of Gd concentration for the four combined detectors. Where the cortex and medulla have different concentrations. The combined $K\alpha_1$ and $K\alpha_2$ of Gd is in black and is fit with a linear regression. The slope for the linear fit is $1.679 \times 10^{-7} \pm 6.835 \times 10^{-10}$ 80

List of Tables

2.1	Summary between the liver and kidney phantoms. The liver having a higher volume will need more Gd compared to the kidney phantom. Although, the kidney phantom is more efficient in terms of MDL due to the smaller size and better positioning for detection.	20
3.1	MDL per detector in ppm for the liver. Detector one has the worse MDL since it has the worse energy resolution of all detectors.	34
3.2	MDL per detector in ppm for the kidney. Detector one has the worse MDL since it has the worse energy resolution of all detectors.	39
4.1	The average peak area, live time, counts, and dead time for all four detectors as the distance increases.	46

4.2	MDL per detector in ppm for the liver. Detector one has the worse MDL since it has the worse energy resolution of all detectors.	47
4.3	MDL per detector in ppm for the kidney. Detector one has the worse MDL since it has the worse energy resolution of all detectors.	52
7.1	Opposite Gd concentrations for the medulla and cortex of the kidney peak areas, for each detector.	81

Chapter 1

Introduction

Gadolinium-based contrast agents (GBCAs) have been used in medical imaging since the 1980's. Magnetic resonance imaging (MRI) incorporates GBCAs for better tissue contrast examinations. GBCAs have a history of dissociating in the body, instead of being excreted through urine a few hours after administration. They are instead stored in several organs such as the brain, bones, kidneys, and liver [23]. Gadolinium (Gd) when free in the body can be toxic. Gd has an ionic charge of +3 in nature and this form is the most common to cause toxicity in the body. Mostly due to its insolubility and ionic radius like Ca^{2+} , where Gd^{3+} competes with Ca^{2+} for the voltage gated calcium channels [21]. All GBCAs have a wide safety margin at low doses in patients with normal renal functions, where most of the cases with reactions to the GBCAs are from patients with a history of asthma, allergies, and renal impairments [21]. Some patients with renal impairments have devel-

oped nephrogenic systemic fibrosis (NSF) after the administration of GBCAs. NSF is a painful medical disease where there is widespread tissue fibrosis in the skin (hardening of the skin), but this is also found in other organs such as the lungs, liver, heart, and muscles [21]. Since renal impairment slows down the excretion of urine, Gd^{3+} dissociates from the chelates and deposits in the body. Most of the NSF cases were found after the administration of Omniscan, OptiMARK, and Magnevist [21]. Around the same time of the discovery of NSF, studies have shown gadolinium retention in bone found in healthy individuals as well as people with normal renal functions [15]. Gadolinium excreted in urine is used as a biomarker for symptomatic patients for monitoring their gadolinium toxicity. Bone and its correlation with urine was studied and it was found that urine and bone Gd concentration do not have a relationship. Also, the urinary Gd concentration was higher in symptomatic patients compared to non-symptomatic. Therefore, gadolinium must be retained in the body by other organs [15], which is why the liver and kidneys are prime target organs of this research.

1.0.1 Gadolinium

Gd is a lanthanide of transition metal and has an atomic number of 64. It has strong paramagnetic properties due to its 7 unpaired electrons. Therefore, it has strong hydrogen proton spin-lattice relaxation effects which can be used to improve contrast between healthy and diseased tissue [13]. The paramagnetic properties allow Gd to be used in a clinical setting, with con-

trast agents for MRI. The magnetic moment of an unpaired electron is much stronger than the magnetic moment of a nucleus [14]. Therefore, Gd increases the dipole-dipole interactions in the spin-lattice, leading to a faster rate of relaxation of the T1 relaxation time (longitudinal relaxation), giving better contrast between healthy and diseased tissue. The ultimate contrast agent for MRI needs to be a solution that is non-toxic, has strong paramagnetic effects, stays stable in the body, and has great tissue specific distribution [14].

Gd is found in an oxidized form in nature, with an oxidation state of +3. Gd^{3+} is highly toxic and can be deposited in certain organs and obstruct calcium ion channels in muscles and nerves [14]. Gd^{3+} is a known competitor for Ca^{2+} due to their similar atomic radii. Gd^{3+} also impedes biological processes in the body, where it binds to phosphates and hydroxides in blood, which is then found in the liver [14]. To prevent these effects, Gd^{3+} is attached to a chelate complex. Since tumour tissue is physiologically different from healthy tissue, it allows for the permeability of much larger molecules. Therefore, it can take more contrast agent compared to healthy tissue [14]. There are two different classes of chelate complexes with Gd such as the macrocyclic molecules, where the Gd^{3+} is enclosed by ligands in a tight bond, and linear molecules, where Gd^{3+} is wrapped by ligands that are long organic molecules [13]. The ligand that binds with Gd^{3+} and that is most commonly used is diethylenetriaminepentaacetic acid (DTPA) [14]. The GBCAs are composed of a chelate class either macrocyclic or linear, a charge either ionic or non-ionic, and stability either thermodynamic or ki-

netic [13]. A macrocyclic chelate such as gadoterate meglumine (Dotarem) and gadoterical (ProHance) are more stable than linear chelates. Non-ionic solutions are less stable when compared to ionic solutions. Therefore, the most stable contrast agents are the ionic macrocyclic chelates and the least stable are the non-ionic linear chelates [13].

There are concerns with GBCAs where endogenous ions can compete with Gd^{3+} and cause transmetallation (the paramagnetic ion is expelled from the complex) [12]. The most competitive elements are Zn^{2+} , Cu^{2+} , and Ca^{2+} . When replacing Gd in the chelate, the Gd will be released in the body and most likely found in the liver and kidneys [12].

1.0.2 Nephrogenic Systemic Fibrosis

Nephrogenic systemic fibrosis (NSF) first appeared in 1997, raising suspicion that introduced agents might be the reason. NSF is a disorder where there is a widespread tissue fibrosis. It is known to occur in patients with renal disease and can sometimes develop rapidly [10]. NSF is the increased tissue deposition of collagen, causing hardening and thickening of the skin of the extremities, muscle weakness, and generalized pain. This can result in immobility and contractures of the joints. In extreme cases, patients may have other tissues involved as in the lungs, skeletal muscles, heart, diaphragm, esophagus, etc. [10]. NSF can also result in immense morbidity and mortality in extreme cases [7]. The presence of the NSF symptoms only appear between 2-4 weeks after an MRI with GBCA administration [6]. Through

decades of research, the mechanism of NSF has not been elucidated. There are not any cures for NSF other than correcting the renal functions with surgery or using other medical means. According to a small study in Austria, the administration of GBCAs for MRI has been associated with some patients with NSF [10]. Another case in Denmark where a study with approximately 400 patients with severe renal disease were administered GBCAs for MRI. As a result, 5 % of the patients were then diagnosed with NSF [10]. Patients with renal disease that developed NSF indicated that the GBCAs were not clearing from the body within the expected hour after administration. Patients with renal disease have prolonged the release of GBCAs for 30-120 hours according to pharmacokinetics studies [6]. Therefore, there is a correlation between NSF and GBCAs since Gd was found to be deposited in the skin of patients with NSF. Research also proves that patients with NSF had more detectable Gd in their urine, therefore it is stored in the body somewhere [14]. Thus, a set of precautions were established to prevent NSF for patients with renal disease, which were to immediately do dialysis after GBCA administration, or to completely avoid the use of a contrast agent for MRI [14]. A recent case in 2013 has shown the prevalence of Gd in the brains of patients that have completely healthy kidneys, meaning there are even more concerns of Gd retention in the body and its safety of GBCAs for MRI [14].

1.0.3 Gadolinium Measurements in Humans

The concerns of Gd retention in the body have led to the need of a non-invasive method of measuring Gd *in vivo*. Previous methods of detection have shown to be quite invasive. For bone measurements, bone specimens and autopsy samples were taken from patients who were undergoing hip replacement surgery [26]. Using a method called inductively coupled plasma mass spectroscopy (ICP-MS), the Gd concentration in bone can be measured. It is a highly effective method of Gd detection, but it destroys the bone sample during the measurement [14]. Another region of accumulation for Gd from GBCAs is the brain. A lot of research has been conducted with bone and brain samples using the ICP-MS method of detection. Various autopsy samples from the different areas of the brain were taken and were measured with the ICP-MS method. The brain samples came from the patients that underwent several MRI with GBCAs and had regular renal function [17]. Gd was found in the brain samples, therefore, Gd de-chelated and is a concern for potential toxicity. In addition, it proves a linear relationship between Gd concentration, and the number of multiple doses administered over time [17]. Also, Gd concentration in the brain has concluded to be proportional to Gd concentration in bone [17]. Therefore, the concentration in bone could potentially be compared to brain concentrations when used in a clinical setting. The X-ray Fluorescence (XRF) technique does not destroy the bone sample, it can measure the Gd in the bone using an *in vivo* method [14]. A successful study of bone measurements using the XRF method would be useful in

a clinical setting and could relate to their brain Gd concentration as well. This study examined the efficiency of Gd detection using an XRF detection system. A patient can simply put their leg in front of the detector for 30 minutes and the concentration of Gd can be determined [14]. Another method of detection is neutron activation analysis. Since Gd has a large neutron capture cross section it would seem to be an ideal candidate for this method. It is a trace element analysis technique. The Gd-157 absorbs the neutron and forms an excited state of Gd-158. The gamma-rays emitted from the de-excitation of the Gd-158 can be used for activation analysis [5].

1.0.4 X-Ray Fluorescence

X-ray fluorescence (XRF) utilizes the photoelectric effect, which is a process between electrons and photons. Photons are electromagnetic radiation and can disperse energy through three different processes, the photoelectric effect, Compton scattering, and pair production [11]. The photoelectric effect is where the energy from a photon or gamma-ray (electromagnetic radiation), interacts with an atomic electron. The energy of the photon is transferred to the electron. The electron is then ejected from the atom. The energy of the emitted electron (E_e) is equal to the energy from the incoming photon ($h\nu$) minus the binding energy of the electron (ϕ) [11].

$$E_e = h\nu - \phi \tag{1.1}$$

When an electron from the inner atomic shells (K or L) is ejected, the electrons from the shells above will fall from their higher energy states to fill the hole of the initial electron [11]. This results in a release of energy called an x-ray. X-rays are similar to gamma-rays, but gamma-rays originate from the energy transformations of the nucleus of an atom where x-rays are from the atomic electrons [11]. When an electron from an inner shell leaves a vacancy, an electron from an outer shell transitions down to fill it. Therefore, there is a series of electrons performing transitions to fill those vacancies. Each of them results in an emission of an x-ray. The x-rays energies are specific to their shell (K, L, M, N). These photon x-rays can be assigned a subscript that help identify the shell where the electron vacancy was filled (α, β, γ , etc). In the case of Gd, it has an x-ray coming from an electron transition of the L shell to the K shell, this is named $K\alpha$ [11].

XRF uses photons to fluoresce atoms of the elements in question, in this case Gd. The atom then emits x-rays that have energies that are specific to that element of interest. The number of x-rays is going to be proportional to the number of atoms of the element in the sample [25]. The *in-vivo* XRF technique originated from measurements on iodine in thyroid in 1968. The first measurements using the Cd-109 source for Pb in bone measurements started with Laird et al. in 1982. David Chettle and Andrew Todd reviewed *in-vivo* XRF measurements in 1994 using a Cd-109 source that emits 88.035 keV γ -rays. They were performed for 30 minutes with patients sitting in a chair, the XRF detection system was placed accordingly and the radiation

detectors were suited to the energy of the radiation emitted, therefore hyper-pure germanium (HPGe) for K-XRF [25]. The current detection system used in this thesis work, originated from the bone Pb experiments. The Cd-109 activation source was investigated instead of using the original source for *in-vivo* bone Pb XRF, which was Co-57 [18]. Cd-109 resulted in a better detection limit compared to Co-57 by a factor of 12. The detection efficiency was also improved by adding another 3 HPGe detectors to the system, thus having four 16 mm HPGe detectors with four sets of electronics. This design arose from Monte Carlo simulations, of bone Pb phantoms [18]. Since bone Gd measurements were successful using the K-XRF method, the next organs of interest liver and kidney, known as storage sites for GBCAs, will be studied in this thesis work.

1.0.5 Detection System

As mentioned above, a study conducted by Nie et al., 2006, determined an improved XRF technique for Pb in bone utilizing four HPGe detectors. They are a type of semiconductor detector, that are chosen for high-energy γ -ray studies. Semiconductor material utilizes the electron-hole pair process, which collects charges produced by the ionization of the material. An electron-hole pair is produced and is drawn by an electric field to the anodes, generating a pulse (Figure 1.1). Impurities in the germanium have been inserted to lower the energy needed to create the electron-hole pairs. Germanium detectors have a valence of 4 and impurities of either a valence of 3 (acceptor) or 5

(donor) will exist in the crystal [8]. When there are acceptor impurities, a detector is called p-type and where there are donor impurities, then the detector is classified as an n-type detector. There is a concept called reverse biasing where there is no current passing through the detector. Holes from the p-type material will migrate towards the electrons from the n-type material and vice-versa [8]. This p-n junction created with the impurities will polarize the reverse biasing. Between the p and n junction, there is a depletion layer. This is where a few charge carriers remain imitating a pure semiconductor [8]. Once the voltage is applied, there is a high enough electric field that the depleted region will make a feasible semiconductor detector. The depleted region is sensitive to x-rays and γ -rays and therefore the depletion depth determines the detectors performance, where the depth is inversely proportional to the total impurity concentration in the detector [8].

There are several detector configurations that can be used for optimal detection efficiency. In this thesis work, the detector was planar. It has a cylindrical p-type crystal with an n-type and p-type electrical contact creating a p-n junction between the crystal and electrical contact (Figure 1.2) [14]. As mentioned, this thesis work uses a HPGe, which means it is a detector with a high atomic number with low impurity concentrations. This would decrease the amount of energy (approximately 3 eV) required to produce an electron-hole pair. The electric field in these types of detectors determine the velocity of the charge carriers caused by the ionization radiation. This is important for the pulse shaping, timing, and charge collection process [9].

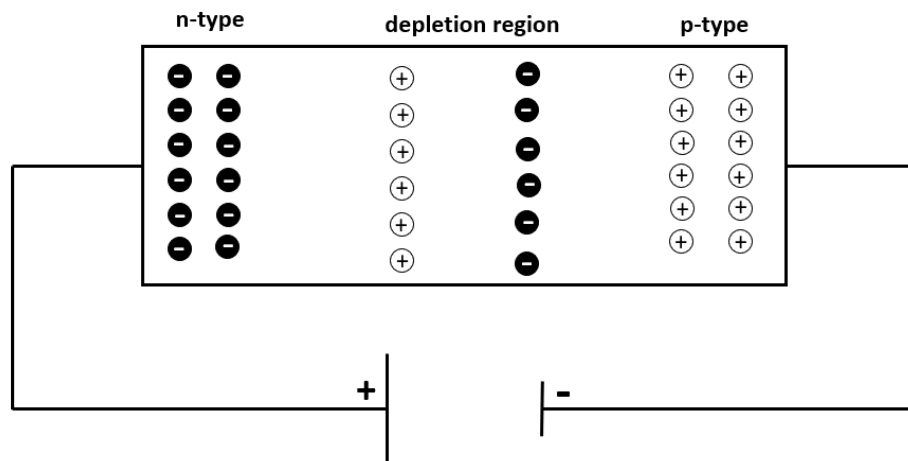


Figure 1.1: Depletion region for a germanium semiconductor crystal. Also called a p-n junction between the two p-type and n-type semiconductor materials. The charge carriers are pulled away from the depletion region when a negative bias is applied.

As for the energy resolution from germanium detectors, they are very dependent on the number of charge carriers, the efficiency of charge collection, and electronic noise [9]. The full width at half maximum (FWHM) is one measure of the quality of the detector. Once the charge carriers advance to the electrodes, the charge is then collected in a preamplifier. The preamplifier has a feedback capacitor, which amplifies the sensitivity of the input so that it is unaffected by other external capacitance changes. The time resolution from germanium detectors are dependent on the overall average rise time and the significant variation in the pulse shape from event to event [9].

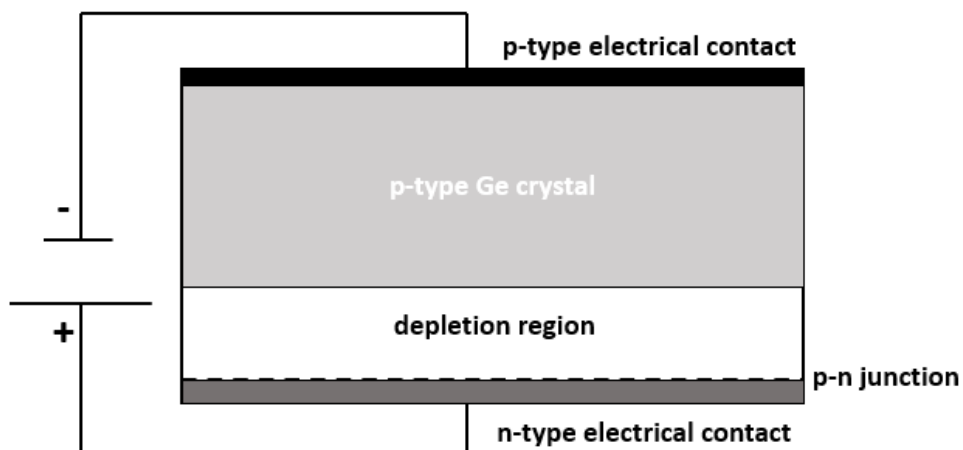


Figure 1.2: Planar detection configuration with a larger depletion region specific to a HPGe detector.

Since there is a small bandgap for HPGe, operation at room-temperature would be impossible since there would be a lot of leakage current. Ge detectors must be cooled to a temperature of 77 K to reduce leakage current

where the noise does not ruin their excellent energy resolution. There is an insulated dewar for liquid nitrogen that kept the detector at the steady low temperature [9].

1.0.6 Excitation Source

As mentioned above, a Cd-109 excitation source is used for bone Pb XRF because it provides a better detection limit. This source emits 88 keV γ -rays which can excite the Gd present in the phantoms. Figure 1.3, displays the decay scheme of Cd-109. Cd-109 decays to Ag-109 following electron capture (EC) at 100 %, resulting in Ag-109m (half-life of 39.8 seconds), which immediately goes through de-excitation. The γ transition of this Cd-109 decay only occurs 3.7 % of decays compared to undergoing internal conversion 96.3 % (IT) of the time [19]. The Cd-109 source can act almost as a point source when exciting Gd because the source can be made to a very small size. Cd-109 has a half-life of 464 days, therefore it can be used for a few years [19].

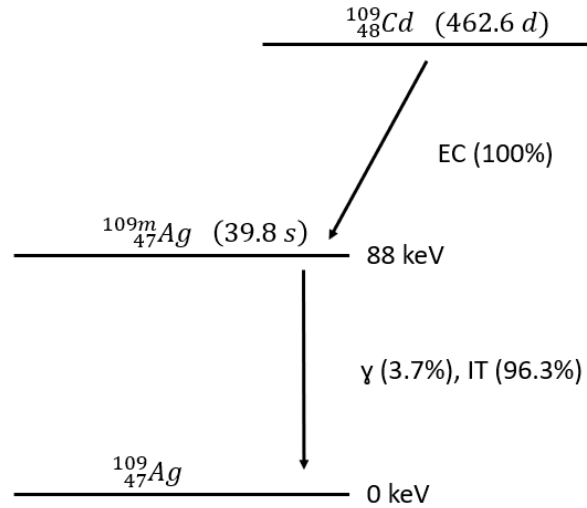


Figure 1.3: Decay scheme of Cd-109.

1.0.7 Detection of Gadolinium using XRF

There are two different characteristic x-rays that are examined when looking at the detection of Gd using XRF. The $K\alpha_1$ x-ray of 42.996 keV is expelled from an electron transitioning from the L_3 shell to the K shell of the atom. The second characteristic x-ray is $K\alpha_2$ with an energy of 42.308 keV. This x-ray is expelled by the transition of an electron from L_2 shell to the K shell. The atomic orbitals can be observed in Figure 1.4. The subscript that is displayed on the L shell is from the different subshells and total angular momentum j [14].

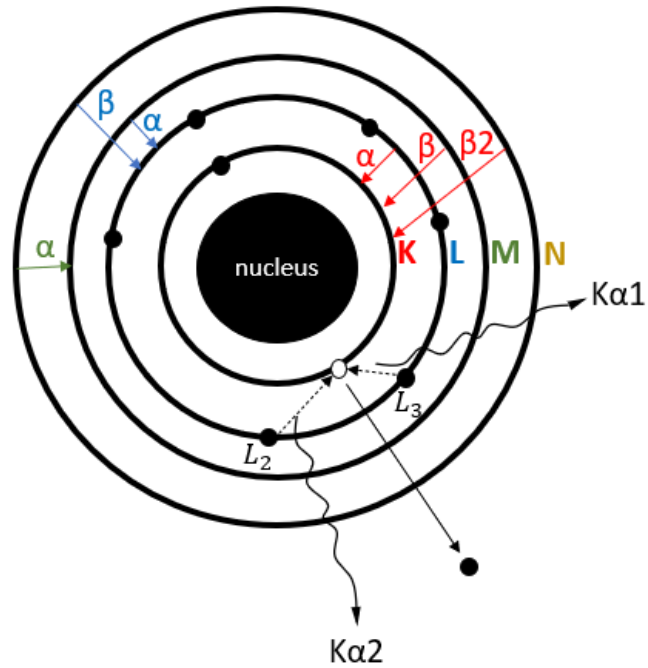


Figure 1.4: This is an example of an atom with varying electron shells. The K shell series is observed with the red and is associated in the case of the two characteristic x-rays for Gd. The $K\alpha_1$ x-ray of energy 42.996 keV is the resultant from the transition of an electron moving from L_3 shell to the K shell. As for $K\alpha_2$, of energy 42.308 keV, is the resultant x-ray from an electron transitioning from the L_2 shell to the K shell [14]. There are also $K\beta$ x-rays emitted but since they are higher in energy than the $K\alpha$ series and buried in the Compton continuum, they are not useful for this analysis.

Chapter 2

Methods

2.0.1 Liver Phantoms

Liver phantoms were created for the thesis work. They had varying concentrations of Gd to test the Gd detection using the K-XRF detection system. The phantoms were 2 L plastic scientific bottles made from Nalgene. The bottles were filled with deionized water to represent the water equivalent tissue of the liver. Multiple phantoms of varying Gd concentrations were measured as surrogates for the liver, as well as measurements with varying overlaying thicknesses of water to model the varying tissue thicknesses over the liver observed in people. These measurements are to ensure a good detection limit, allowing the use for human measurements in a clinical setting.

For the liver Gd concentrations, these were chosen arbitrarily. Due to low concentrations of Gd detected through other methods in *in vitro* samples, I had more phantoms with lower concentrations of Gd. Therefore, the

low concentrations are a point of interest. Gd has been detected in *ex vivo* samples using the method of inductively coupled plasma mass spectroscopy (ICP-MS) and *in vivo* in leg muscle using prompt γ neutron activation analysis or in tibia using K-XRF. The bone measurements have resulted in a minimum detection limit (MDL) of around 1.34 ppm [14]. The levels observed in people exposed to gadolinium contrast agents were found to be low with levels often near this detection limit. I have made 6 liver phantoms with concentrations of 0 ppm, 4 ppm, 12 ppm, 25 ppm, 50 ppm, 100 ppm Gd, where the units parts per million (ppm) is equivalent to the μg Gd/g liver phantom. As mentioned above, the liver phantoms are 2 L plastic scientific bottles from Nalgene. They have a wall thickness of 1.0 ± 0.5 mm. They are a cylindrical shape with a lid (Figure 2.1). Phantoms were made using standard addition methods from Gd stock solution which has a concentration of 1000 mg/L Gd in 2 % nitric acid (Sigma Aldrich, Darmstadt, Germany). It was prepared with high purity of Gd_2O_3 , HNO_3 and water. This solution also has 2 ml of nitric acid added into the phantom to prevent plating out the Gd on the phantom walls.



Figure 2.1: 100 μg Gd/g liver phantom bottle.

2.0.2 Kidney Phantoms

The kidney phantoms are smaller but in other respects similar to the liver phantoms. They have a volume of 125 ml and are in a cylindrical form with a lid. They are filled with the same dilutions of the Gd stock solution as the liver, with the added nitric acid and deionized water. They have varying concentrations of 0 ppm, 5 ppm, 10 ppm, 25 ppm, 50 ppm, 100 ppm, where ppm is equivalent to the μg Gd/g kidney phantom. Again, there are a lot more phantoms with lower concentrations of Gd for the kidney phantoms due to the low levels detected of Gd both *ex* and *in vivo* using other methods of detection. To summarize the differences between the two type of phantoms, kidney and liver, see Table 2.1.

Liver (2L)		Kidney (0.125L)	
$\mu\text{g/g}$	mg	$\mu\text{g/g}$	mg
0	0	0	0
4	8	5	0.625
12	24	10	1.25
25	50	25	3.125
50	100	50	6.25
100	200	100	12.5

Table 2.1: Summary between the liver and kidney phantoms. The liver having a higher volume will need more Gd compared to the kidney phantom. Although, the kidney phantom is more efficient in terms of MDL due to the smaller size and better positioning for detection.

2.0.3 Torso Phantom

The liver and kidney phantoms are in the torso portion of the human body. Since the human body is made of 65 % water along with other minerals, water was used to simulate the human body [3]. Therefore, a torso phantom was added to the experiment (Figure 2.2). The bucket of water has dimensions of 51 ± 0.5 cm in height, 52 ± 0.5 cm in length, and 35 ± 0.5 cm wide. It has a wall thickness of 5 ± 0.5 mm. It is filled to the top with water that is not distilled. The liver and kidney phantoms were submerged into the torso phantom in positions that model placement in humans and held in place with retort stands and clamps. Therefore, the Gd detection is simulated as if detecting a human body.



Figure 2.2: Human torso phantom with the liver phantom lowered into the cavity, making it the ideal experimental set-up.

2.0.4 Overlaying Tissue Thickness

Due to the varying sizes of the human body, different overlaying tissue thicknesses have been observed over the liver and kidneys. To vary the tissue thickness, the phantoms were simply moved further from the wall that was facing the detector, inside the torso phantom. The thicknesses measured are 5 ± 0.5 mm (up against the torso wall), 10 ± 0.5 mm, 15 ± 0.5 mm, 20 ± 0.5 mm, 25 ± 0.5 mm. The phantom assembly was placed 1 ± 0.5 mm from the source to the bucket of water and the torso wall thickness of 5 ± 0.5 mm, which is why the first measurement started at 5 mm and not 0 mm.

2.0.5 The Source

A Cd-109 source was used for the XRF measurements (please refer to Figure 1.3 for detailed source information). It is a small cylinder with dimensions of 3 mm length and 3 mm diameter. There is a 1.1 mm active diameter of Cd-109 and it is backed by a Ag plug. It is enclosed in a capsule made of W and is placed in a Pd collimator. The collimator has a copper face to filter out the silver x-rays from the radio-daughters in the decay chain. Cd-109 has a half-life of 464 days. The initial activity was of 5 GBq, but had decayed over time therefore, the activity for the phantom measurements started at 0.78 GBq. The 88 keV γ -rays are emitted from the Cd-109 source, the copper filter almost completely eliminates the silver x-rays, only allowing 0.10 % to escape. The source faces the copper filter. The source is then placed in a

plastic holder on the face of the detector (Figure 2.4). The source is placed at an angle of 180° resulting in a Compton peak from the 88 keV γ -rays. The Compton peak was found experimentally at approximately 67 keV. This means the scattering angle is not exactly 180° , due to the size of the body phantom, therefore, the angle is 145° (Figure 2.3).

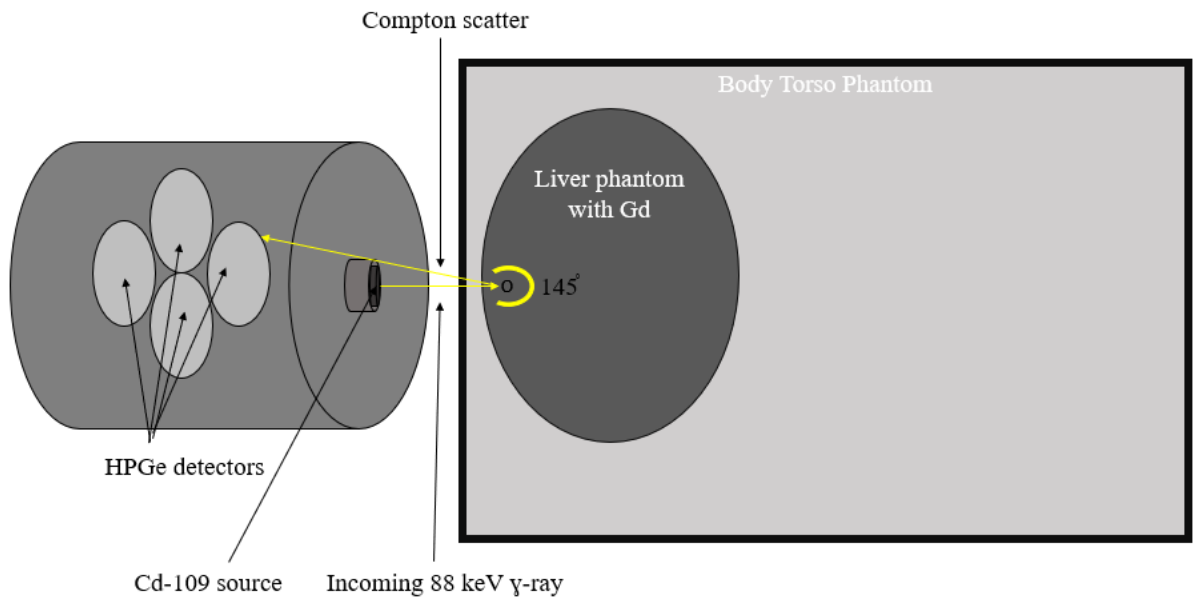


Figure 2.3: The measurement geometry is near backscatter, the source-detector to the front of the liver or kidney phantom is the only distance that needs to be varied. The source-detector to front of torso phantom can stay constant.

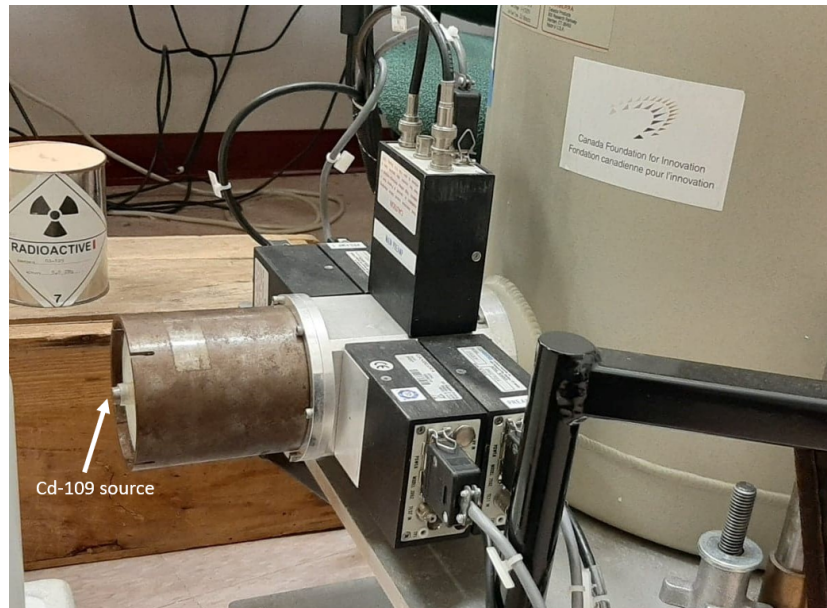


Figure 2.4: Cd-109 source placed inside its capsule, with a copper face, then placed in the plastic holder in front of the face of the detectors.

2.0.6 The Cloverleaf HPGe Detection System

The cloverleaf K-XRF detection system is composed of 4 HPGe detectors with 4 separate sets of electronics to permit use of a high activity Cd-109 source. This detection system is able to process high count rates. Due to the high count rate from the Cd-109 source, a process called a pile-up occurs which means new voltage pulses build onto the exponential decay of the previous event. Therefore, the preamplifier cannot return to the baseline voltage. Events can be mis-recorded as being a higher energy event and can saturate the pulse processing electronics. This affects the detection of other output from any subsequent pulses.

The name “cloverleaf” is used since the detectors are placed in a cloverleaf formation inside the aluminum can (Figure 2.5). They are 200 mm² with a thickness of 10 mm (Canberra GL0210R/S). They are each connected to their own preamplifier (Canberra 2002CP), and a DSA 1000 pulse processing system. The software used for the energy spectrum of each detector is Genie 2000 Gamma Analysis Software. The energy spectra are then analysed using MATLAB (The MathWorks Inc, MATLAB R2019b).

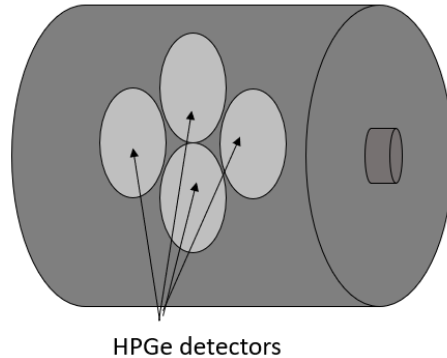


Figure 2.5: Detector face with the plastic holder. Inside there are the four HPGe detectors in a “cloverleaf” formation.

Each of the energy spectra from the liver + torso phantom, or kidney + torso phantom has distinct features. The Gd $K\alpha_2$ and $K\alpha_1$ x-ray peaks are situated at 42.308 and 42.996 keV respectively and are mostly unidentifiable to the human eye for the very low concentration phantoms (0-15 ppm). Therefore, a peak fitting analysis is used with MATLAB algorithms for each energy spectrum from each detector. A mathematical model is fitted to the spectrum. In this work, the fit consisted of a double Gaussian

function to model the x-ray peaks and a fourth-order polynomial to model the background (Figure 2.6).

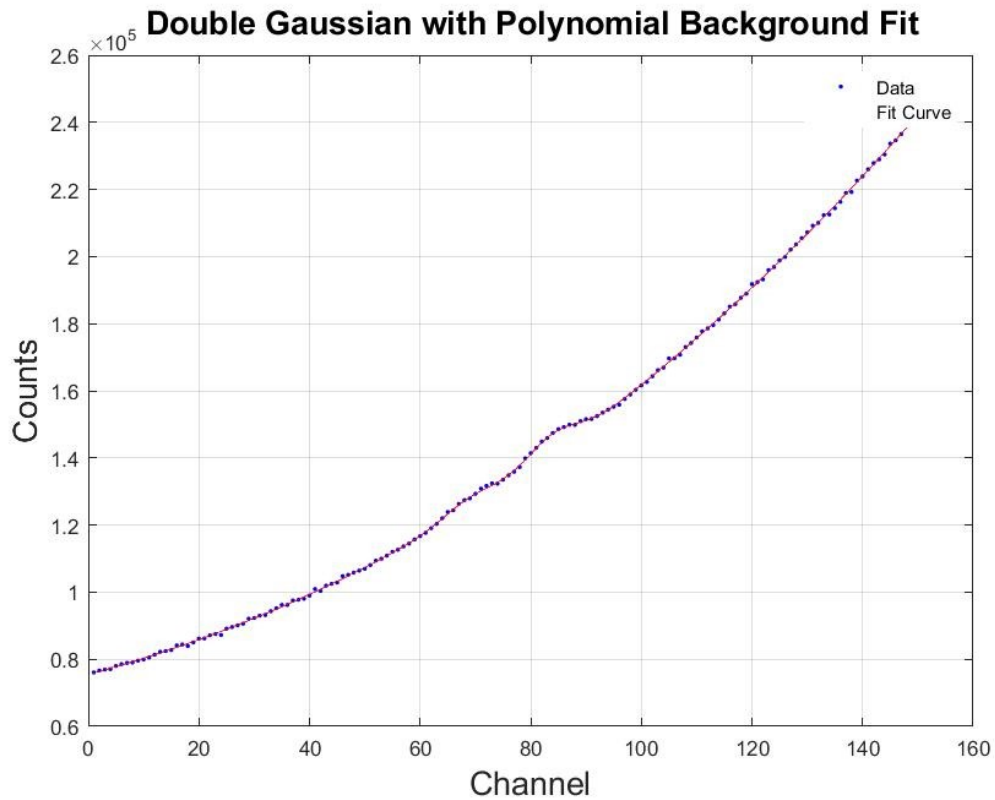


Figure 2.6: Double Gaussian peak fitting to the two Gd $K\alpha_2$ at 42.308 keV and $K\alpha_1$ peaks at 42.996 keV, with a fourth-order polynomial background fit. The blue dots are the data points from energy spectrum of detector 4. This is the experimental measurement of the kidney phantom at $100 \mu\text{g Gd/g}$ phantom, and the red line is the fit.

The code used the MATLAB function “fitype”, which the user can create a custom Nonlinear Model, in this case a Nonlinear Least Squares fit. The equation below is the best fit found for the two Gd peaks and the background:

$$y = p_1x^4 + p_2x^3 + p_3x^2 + p_4x + p_5 + 0.556 a_2 e^{-\frac{1}{2}\left(\frac{x(b-b_1)}{c}\right)^2} + a_2 e^{-\frac{1}{2}\left(\frac{x-b}{c}\right)^2} \quad (2.1)$$

Where, y is the peak area plus the background fit, p_1 , p_2 , p_3 , p_4 and p_5 are constants for the polynomial background fit, a_2 is the height of the two combined Gd peaks, c is the width of the two peaks combined. Where the first peak (a_2) is calculated to have an amplitude 0.556 times the amplitude of the second peak (a_1). The centers of the peaks have been combined, where the first peak needs to be adjusted due to the center being different than the second peak, which is the variable b , and b_1 . Since there are many parameters to this equation, the number of parameters were reduced as much as possible to lower the uncertainties from the fit. This included linking the positions of the two Gd peaks, and thus determining the position of one peak. In addition, the widths of the Gaussian peaks were fixed.

2.0.7 Minimum Detection Limit

The minimum detection limit (MDL) is the minimum number of counts that can be confidently considered to be larger than the statistical variations in the background signal. I followed the MDL approach from Lord, M. (2019). The calibration lines from the peak area of the combined two peaks of Gd along with the concentration of the phantoms created calibration lines for both the kidney and liver phantom data (Figure 2.7).

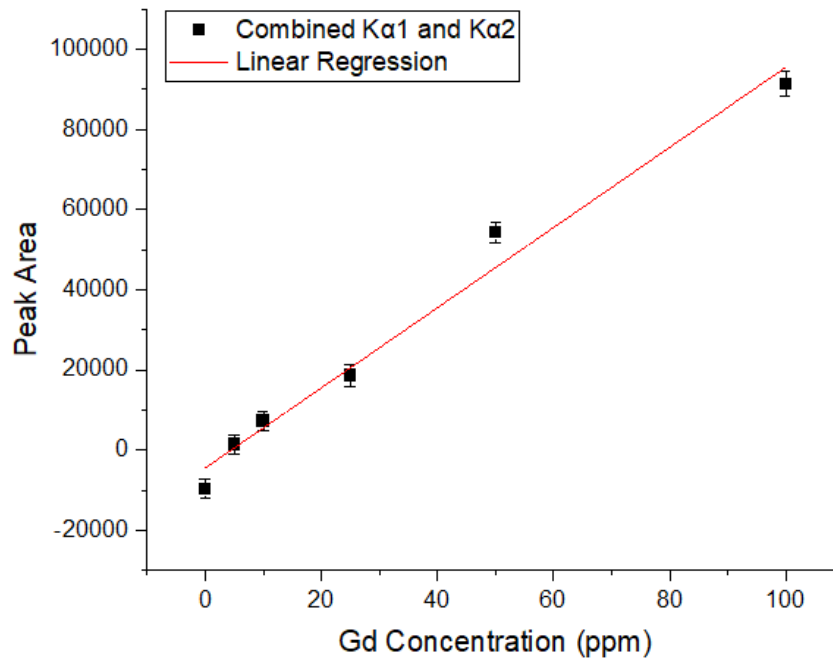


Figure 2.7: Kidney phantom calibration line where the peak area is plotted against the phantom concentrations of Gd. A linear regression analysis fit the data points. The intercept is negative since the peak areas are subtracted by the background. The Gd concentration does have an error, but the error bars are not visible since they are small. The Gd concentration error stems from the pipette (P1000), pipette (P200), as well as from a graduated cylinder.

The calibration lines follow a linear relationship, therefore:

$$y = mx + b \quad (2.2)$$

Where y is the peak area, m is the slope of the calibration line, x is the Gd concentration, and b is the intercept of the calibration line. The calculation to find the uncertainty of the Gd concentration is the minimum detection limit that is of interest :

For a measured $y \pm \delta y$, the unknown \hat{x} is given by $\hat{x} = \frac{y-c}{m}$.

Then $\sigma_{\hat{x}}^2$ is given by:

$$\begin{aligned} \sigma_{\hat{x}}^2 = & \left(\frac{\delta \hat{x}}{\delta y} \right)^2 \sigma_y^2 + \left(\frac{\delta \hat{x}}{\delta c} \right)^2 \sigma_c^2 + \left(\frac{\delta \hat{x}}{\delta m} \right)^2 \sigma_m^2 + 2 \left(\frac{\delta \hat{x}}{\delta y} \right) \left(\frac{\delta \hat{x}}{\delta c} \right) \text{COV}_{y,c} \\ & + 2 \left(\frac{\delta \hat{x}}{\delta y} \right) \left(\frac{\delta \hat{x}}{\delta m} \right) \text{COV}_{y,m} + 2 \left(\frac{\delta \hat{x}}{\delta m} \right) \left(\frac{\delta \hat{x}}{\delta c} \right) \text{COV}_{m,c} \end{aligned}$$

Where $\text{COV}_{y,c}$, $\text{COV}_{y,m}$, $\text{COV}_{m,c}$ are covariances. Since the areas of the peaks are independent of the slope and intercept of the calibration line, then the covariances $\text{COV}_{y,c}$ and $\text{COV}_{y,m}$ equal zero.

Taking the partial derivatives from the equation above gives the equations below:

$$\left(\frac{\delta \hat{x}}{\delta y} \right) = \frac{1}{m} \quad (2.3)$$

$$\left(\frac{\delta\hat{x}}{\delta c}\right) = -\frac{1}{m} \quad (2.4)$$

$$\left(\frac{\delta\hat{x}}{\delta m}\right) = \frac{-(y-c)}{m^2} \quad (2.5)$$

Therefore, the equation becomes:

$$\sigma_{\hat{x}}^2 = \frac{1}{m^2}\sigma_y^2 + \frac{1}{m^2}\sigma_c^2 + \frac{(y-c)^2}{m^4}\sigma_m^2 + 2\frac{(y-c)}{m^3}\text{COV}_{m,c} \quad (2.6)$$

The minimum detection limit is then calculated:

$$\text{MDL} = 2\sigma_x \quad (2.7)$$

The MDL was calculated for four different energy spectra per measurement. Therefore, four MDLs were calculated and then combined using the inverse variance weighted mean since the MDL is an uncertainty in concentration:

$$\text{MDL}^2 = \frac{1}{1/\text{MDL}_1^2 + \dots + 1/\text{MDL}_4^2} \quad (2.8)$$

Chapter 3

Results

The energy spectra were collected for each of the 6 phantoms for both the liver and kidney phantoms. They were counted for 5 hours each at a distance of 6 ± 0.5 mm from the front face of the source to the front face of the liver and kidney phantoms. The energy spectra were also collected for a secondary experiment studying varying overlaying tissue thicknesses for a counting time of 5 hours for each of the same sets of phantoms.

3.0.1 Liver Phantoms

The spectra collected were analyzed to determine the combined area of the Gd $K\alpha_1$ and $K\alpha_2$ peaks. The areas were plotted as a function of the known Gd concentration for each phantom. The linear regression of fitted area versus Gd concentration created a calibration line. This allowed for the calculation of the MDL using the calibration line, then it was combined for all

four detectors, giving a combined MDL for the detection system. The calibration line for the liver phantom for the combined detectors can be seen in Figure 3.1. The body torso phantom is quite large causing more attenuation for the incoming 88 keV γ -rays which have to reach the phantom. The liver phantom is also very large which contributes to the increased attenuation of the exiting Gd x-rays. Portions of the phantoms are outside of the field of view of the detectors. Only fits that resulted in a chi-square of 1.0 ± 0.25 counts, were accepted for Gd peak area calculations. The fits for the Gd peaks were found to have an average chi-square of 1.18 (in counts), ranging from 0.93 to 1.41, indicating that a relatively good fitting model is being used. The combined MDL calculated for this experiment is 2.59 ppm. Table 3.1 lists the MDL per individual detector, they are then combined using the inverse variance weighted mean. Adjustments have been made to this MDL. The MDL was adjusted to make 5 hours into a clinically possible time of 30 minutes, where $\text{MDL} \propto \frac{1}{\sqrt{t}}$, where t is the time in seconds. This was in addition to adjusting for a higher activity of 5 GBq (A), instead of the 0.78 GBq (A_0), where $\text{MDL} \propto \sqrt{\frac{A_0}{A}}$, where A is the activity of the new source and A_0 is the activity of the original source. The MDL with the final adjustments is 3.68 ppm.

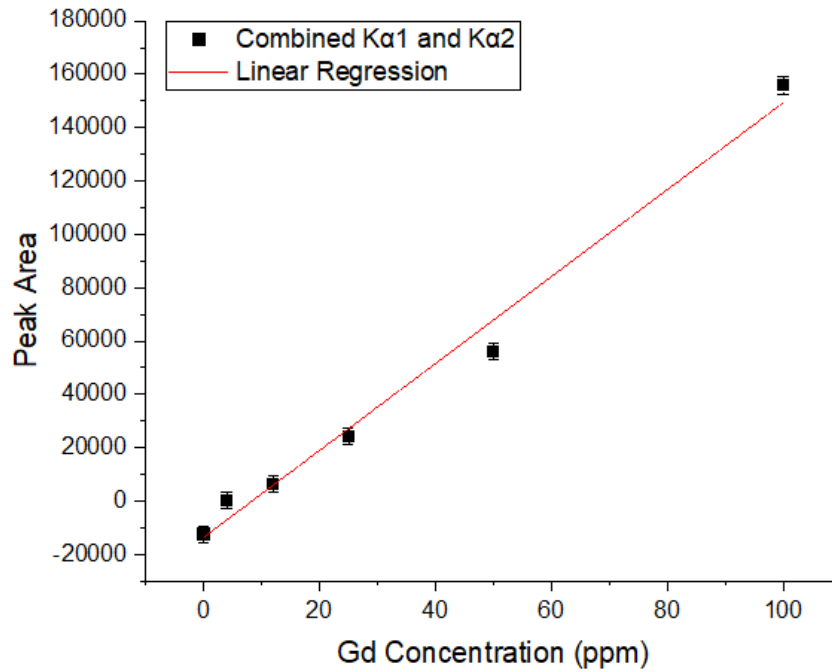


Figure 3.1: Calibration line for the four combined detectors. The measured Gd peak area as a function of the known Gd phantom concentrations for the liver phantoms. It was measured at 6 ± 0.5 mm from the Cd-109 source for a duration of 5 hours. The black is the combined K α 1 and K α 2 peak areas with error bars, fit with a red linear regression. The error bars are small and not easily seen, they reflect only the counting statistics. This line has an R-squared value of 0.98.

Detectors	Minimum Detection Limit (MDL) (ppm)
D1	8.21
D2	5.28
D3	6.02
D4	5.22

Table 3.1: MDL per detector in ppm for the liver. Detector one has the worse MDL since it has the worse energy resolution of all detectors.

3.0.2 Overlaying Tissue Thickness Liver Phantoms

The liver sits in the abdominal region of the body. Therefore, varying tissue thicknesses were observed to accommodate for varying Body Mass Index (BMI) in a clinical setting. Overweight people have a thicker layer of adipose tissue over the liver than a normal or underweight people. The MDL was observed for the varying tissue thicknesses of 6 ± 0.5 mm, 11 ± 0.5 mm, 16 ± 0.5 mm, 21 ± 0.5 mm, 26 ± 0.5 mm. The liver phantom with the highest Gd concentration (100 ppm) was chosen for the experiment due to the visibility of the Gd peaks. The peak area versus tissue thickness is plotted in Figure 3.2. It has a linear decrease; as the thickness increases, the peak area decreases. This was expected due to the phantom moving further away from the detection system. The calculated MDLs were converted into natural logarithmic values since they were following an exponential relationship. They are easily visible when plotted as linear data. The calculated MDLs were

plotted as a function of tissue thickness in Figure 3.3 below, along with the adjusted MDL. As the thickness increases, the MDL also increases. This was expected since increasing the thickness would also increase the attenuation within the water in the torso phantom, detecting less of the Gd in the liver phantom.

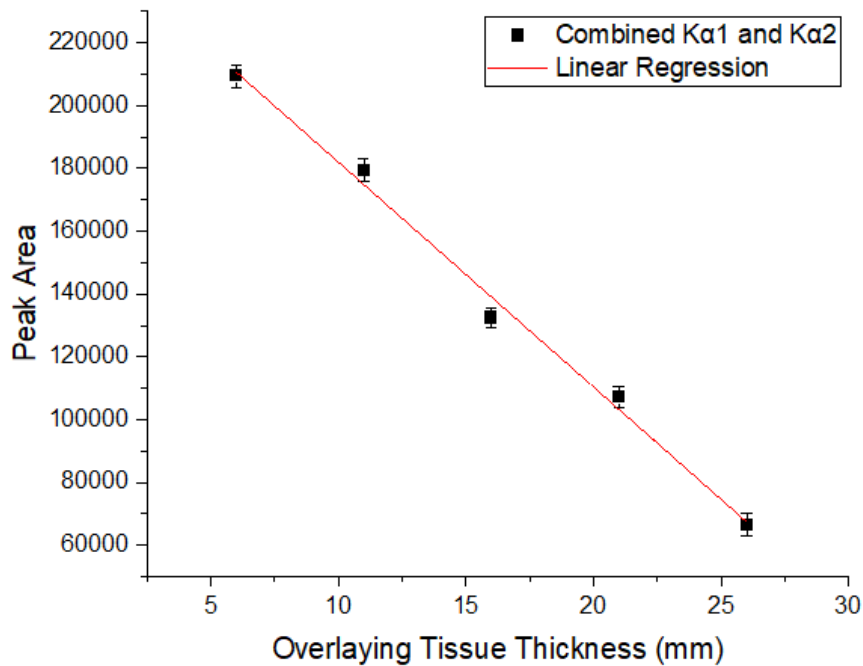


Figure 3.2: Peak area plotted as a function of the overlaying tissue thickness for the MDL calculation. It was fit with a linear regression analysis, in red. The black is the combined Gd $K\alpha_1$ and $K\alpha_2$ with error bars. This is the plot for all four combined detectors.

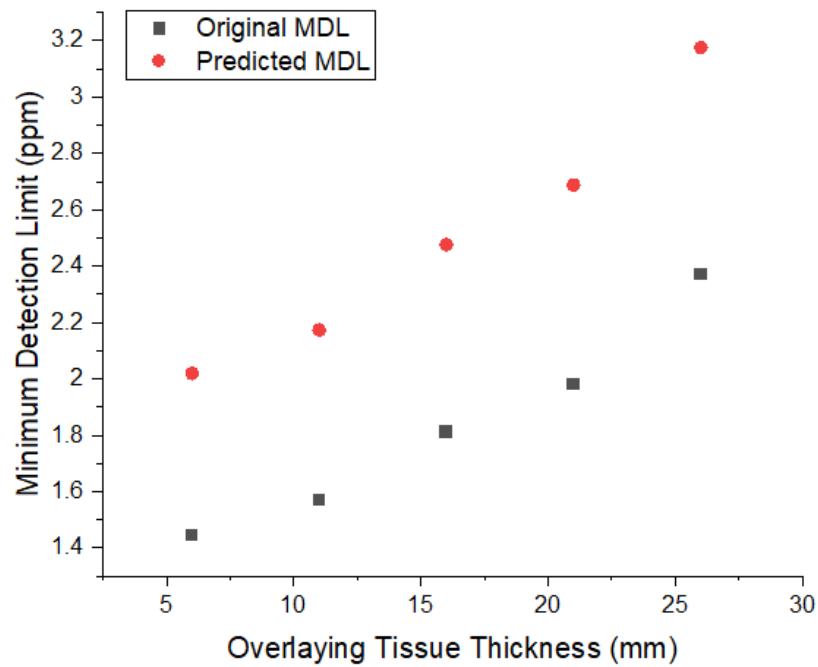


Figure 3.3: Natural logarithmic MDL as a function of tissue thickness for the liver phantoms. The values are the combined Gd peaks $K\alpha_1$ and $K\alpha_2$, where the original MDL is in black and the MDL with the time and activity adjustments is in red. These are the data from all four combined detectors.

3.0.3 Kidney Phantoms

The kidney experiments were similar to the liver experiments. The spectra were collected and analyzed to determine the Gd peaks. The peak areas were plotted as a function of the known Gd concentration. They were fit with a linear regression and they resulted in calibration lines for the calculation of the MDL (Figure 3.4). The MDL was combined from all four detectors, and adjusted due to the time and activity to match a more clinical setting. Table 3.2 lists the MDL per individual detector, they are then combined using the inverse variance weighted mean. A clinical setting is to accommodate for patients undergoing a procedure. An ideal procedure would last approximately 30 minutes, and have a high radioactive source that could accommodate for the 30-minute time. Again the body torso phantom is very large causing a lot of attenuation for the incoming 88 keV γ -rays. The kidney phantom is small which means a lower total mass of Gd making it difficult for the detection of Gd. The fits for the Gd peaks have an average chi-square of 1.20, ranging from 0.82 to 2.87. This again indicates that the mathematical model used to fit the data is relatively good. The MDL calculated for this experiment is based off the combination of three concentrations of 5 ppm, 10 ppm, and 25 ppm, calculating to 3.60 ppm. The same adjustments have been made to this MDL changing the time of 5 hours to 30 minutes and the original activity of 0.695 GBq changed to 5 GBq. The adjusted MDL is 4.26 ppm.

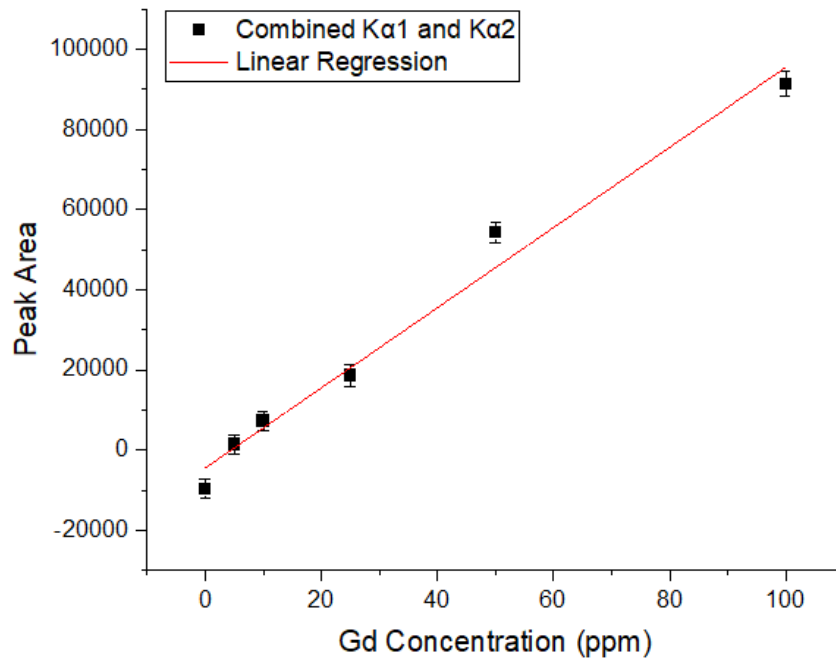


Figure 3.4: Calibration line for the four combined detectors. The measured Gd peak area as a function of the known Gd phantom concentrations for the kidney phantoms. It was measured at 6 ± 0.5 mm from the Cd-109 source for the duration of 5 hours. The black is the combined $K\alpha_1$ and $K\alpha_2$ peak areas with error bars, fit with a red linear regression. This line has an R-squared value of 0.98.

Detectors	Minimum Detection Limit (MDL) (ppm)
D1	8.35
D2	6.32
D3	7.71
D4	7.01

Table 3.2: MDL per detector in ppm for the kidney. Detector one has the worse MDL since it has the worse energy resolution of all detectors.

3.0.4 Overlaying Tissue Thickness Kidney Phantom

The detection of Gd was also observed by varying the tissue thickness. The MDL was observed for each of the tissue thickness, which were the same as the liver tissue thicknesses, 6 ± 0.5 mm, 11 ± 0.5 mm, 16 ± 0.5 mm, 21 ± 0.5 mm, 26 ± 0.5 mm. Again, the phantom with the highest concentration of Gd (100 ppm) was chosen for the experiment. The data accumulated from the experiment were plotted against the tissue thickness. This resulted in an exponential fit analysis, instead of the linear analysis found from the liver phantom, Figure 3.5. The calculated MDLs were plotted as a function of tissue thickness in Figure 3.6, along with the adjusted MDL. As the thickness increases, the MDL also increases, due to the increase in attenuation. It also indicates a potential flattening of the data at the farther distances, meaning the Gd is no longer being detected and/or the attenuation is overpowering the Gd detection.

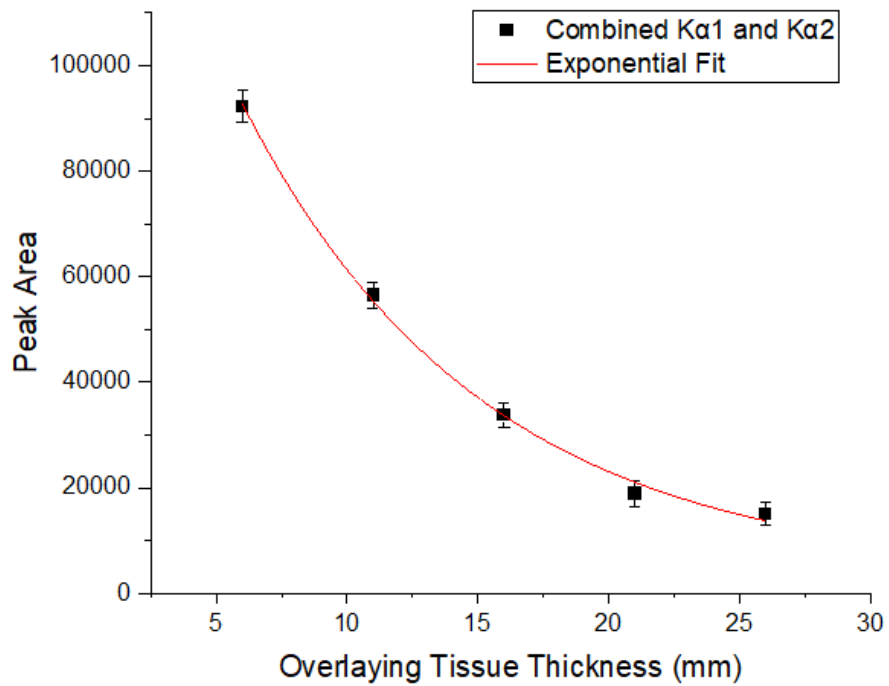


Figure 3.5: Peak area plotted as a function of the overlaying tissue thickness for the MDL calculation. It was fit with an exponential analysis, in red. The black is the combined Gd $K\alpha_1$ and $K\alpha_2$ with error bars. This is the plot for the four combined detectors.

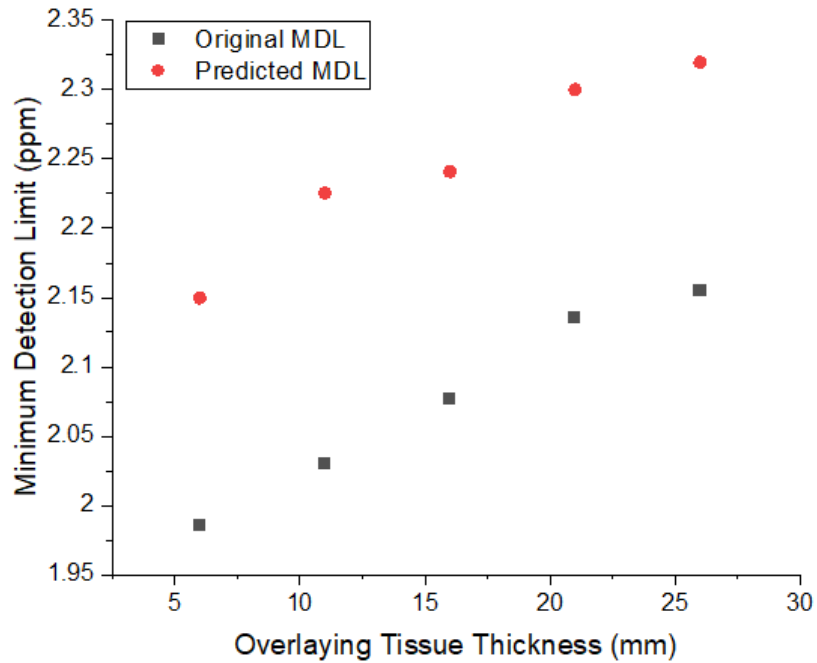


Figure 3.6: The MDL plotted as a function of overlaying tissue thickness. The black is the original MDL and the red is the adjusted MDL. This is for the four combined detectors.

Chapter 4

Results - New Source

Experiments

A source with a higher activity of 5 GBq was used for this section of experiments. A similar set-up as previously described for the colder source was used for the experiments. However, it required a change of source-to-detector distance because putting the water torso phantom with the kidney and liver phantoms of 100 ppm at the distance of 6 ± 0.5 mm saturated the detectors and did not give viable energy spectra. Therefore, an experiment which varied the distance from source-to-detector was performed to determine the optimal distance to run the experiments. The most optimal distance where the detectors were not being saturated, the Gd peak areas were visible, and the peak analysis fit was reasonable, was at a distance of 10 mm from the detector. The water phantom added 1 mm of thickness therefore, the working

distance was 11 ± 0.5 mm from the front face of the source to the front surface of the liver and kidney phantoms. The energy spectra were collected for each of set of phantoms for both the liver and kidney. They were counted for 30 minutes real time. The energy spectra were also collected for a secondary experiment studying varying overlaying tissue thickness for a counting time of 30 minutes real time for each of the same sets of phantoms.

4.0.1 Source-Detector Distance

This distance was determined by satisfying several factors: the dead time, the fit analysis, and the peak area. The distance had to be far enough to have a reasonable dead time. Usually, the dead time should not be more than 40 % however, at that distance the peak areas were not visible, therefore the distance had to be closer to the detector. The figure 4.1 below displays the peak areas as a function of depth with the new source to determine the 11 ± 0.5 mm (10 mm for the water torso phantom from the source plus 1 mm for the thickness of the torso phantom). A gadolinium-based contrast agent (GBCA) vial was put into a waterproof bag and inserted into the torso phantom against the phantom wall closest to the front face of the detector. The GBCA was an Omniscan (gadodiamide) 20 ml bottle, 287 mg/ml of gadodiamide or 0.5 mmol/ml (Figure 4.2). To compare to the liver and/or kidney phantom, this bottle contains 5740 mg of Gd. This high concentration was used because it produced large identifiable x-ray signals in a short time. It was run for 5 minutes real time at each position. The water phantom

distance from the front face of the detector was changed at 5 ± 0.5 mm, 10 ± 0.5 mm, 15 ± 0.5 mm, 20 ± 0.5 mm, and 25 ± 0.5 mm. The data for Figure 4.1 can also be observed below in Table 4.1. The table includes the dead time associated with the peak areas and distances measured. The dead time is defined as the sum of all processing time of the different components in a detection system.

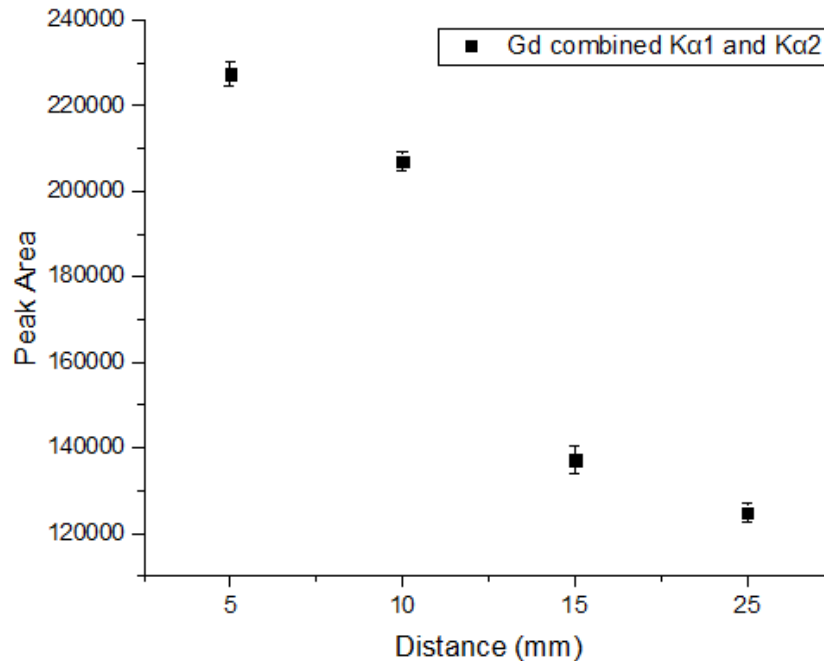


Figure 4.1: Detector 3 peak areas as a function of distance. The error bars are included. The peak areas were small once the distance was past 20 mm but the dead time was reasonable. The peak analysis fit was getting distorted for the distance of 5 mm, therefore the 10 ± 0.5 mm distance for the water torso phantom from the source was chosen. For this distance, the peak area was still high while the peak area analysis fit was not yet distorted. The detectors were not saturated although the dead time was quite large.



Figure 4.2: GBCA available in the laboratory. Omniscan (gadodiamide) in a 20 ml bottle. This bottle was inserted into a plastic bag and then into the water torso phantom for experimental measurements to help determine the source-to-detector distance.

Distance (mm)	Average Peak Area	Average Live Time (s)	Average Counts for Live Time (counts/s)	Average Dead Time
5	170 143.75	88.41	1 924.49	70.53%
10	144 625.25	109.24	1 323.92	63.59%
15	87 250.60	134.49	648.75	55.17%
25	78 584.80	157.26	499.71	47.58%

Table 4.1: The average peak area, live time, counts, and dead time for all four detectors as the distance increases.

4.0.2 Liver Phantoms

The energy spectra were collected and analyzed to determine the combined peak area of Gd $K\alpha_1$ and $K\alpha_2$. The areas were plotted as a function of the known Gd concentration for each phantom. These were fit with a linear regression again creating the calibration lines for the combined Gd peaks. The calibration lines allow for the calculation of the MDL for each detector, which were then combined for a total MDL for the entire detection system. Table 4.2 lists the MDL per individual detector, they are then combined using the inverse variance weighted mean. The calibration line for four combined detectors is displayed below (Figure 4.3). Since the radioactive source is very strong and the set-up had to be backed away, the peak areas are much smaller than the peak areas recorded from the experiment with the weaker source. The torso water phantom is very large and highly contributes to an increased background due to Compton scattering. In addition, there is a $1/r^2$

effect of decreasing Gd signal as the set-up is moved back from the detectors. The fits for the Gd peaks were found to have an average chi-square of 1.18, ranging from 0.96 to 1.61, indicating that a relatively good fitting model is being used. The calculated combined MDL for measurement of Gd in the liver is 3.61 ppm.

Detectors	Minimum Detection Limit (MDL) (ppm)
D1	17.02
D2	10.72
D3	5.09
D4	6.22

Table 4.2: MDL per detector in ppm for the liver. Detector one has the worse MDL since it has the worse energy resolution of all detectors.

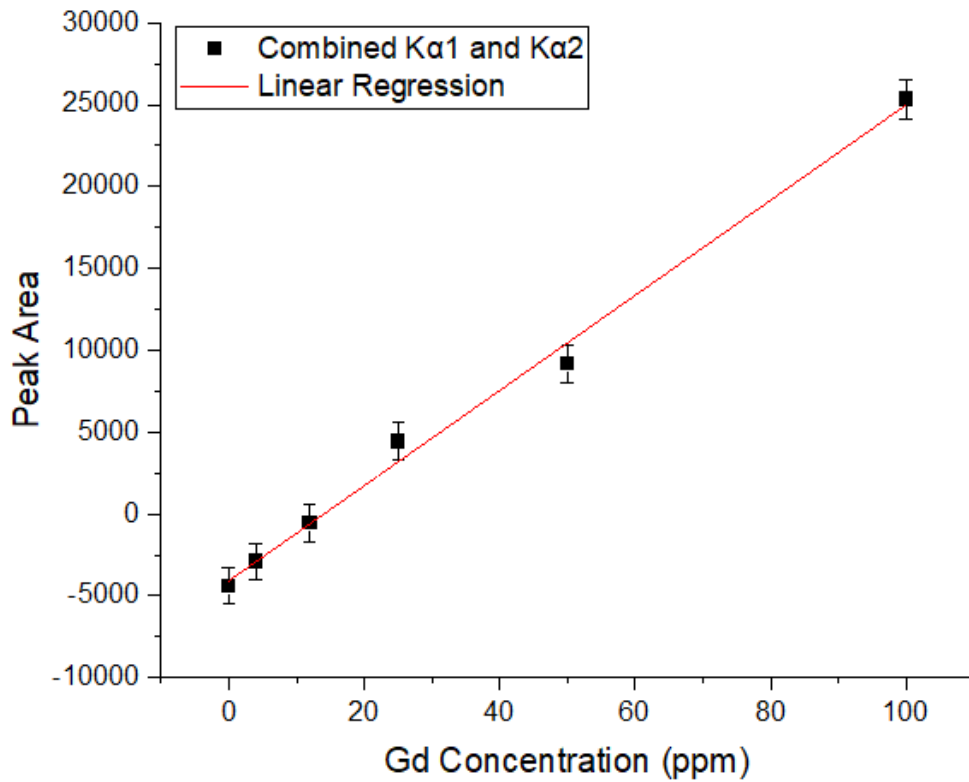


Figure 4.3: Calibration line for the four combined detectors. The peak area as a function of Gd concentration for the liver phantoms. It was measured at 11 ± 0.5 mm from the source for a duration of 30 minutes. The black is combined $K\alpha_1$ and $K\alpha_2$ peak areas with error bars, fit with the red linear regression. This line has an R-squared value of 0.99.

4.0.3 Overlaying Tissue Thickness Liver Phantoms

Varying tissue thicknesses were observed with the new source, to accommodate for varying Body Mass Index (BMI) in a clinical setting. The MDL was observed for varying tissue thicknesses of 12 ± 0.5 mm, 17 ± 0.5 mm, 22 ± 0.5 mm, 27 ± 0.5 mm, and 32 ± 0.5 mm. The 100 ppm liver phantom was chosen to run these experiments due to the visibility of the Gd peaks. The peak areas were plotted as a function of varying tissue thicknesses in Figure 4.4. It has a linear decrease, as the thickness increases the peak area decreases. A decrease was expected due to greater attenuation because of overlying tissue and the Gd in the phantom moving further away from the detection system. The calculated MDLs were converted into natural logarithmic values since they were following an exponential relationship. The MDLs were plotted as a function of tissue thickness in Figure 4.5 below. As the thickness increases, the MDL also increases. This was expected since increasing the thickness would also increase the attenuation of x-rays within the water in the torso phantom, decreasing the efficiency of Gd detection in the liver phantom.

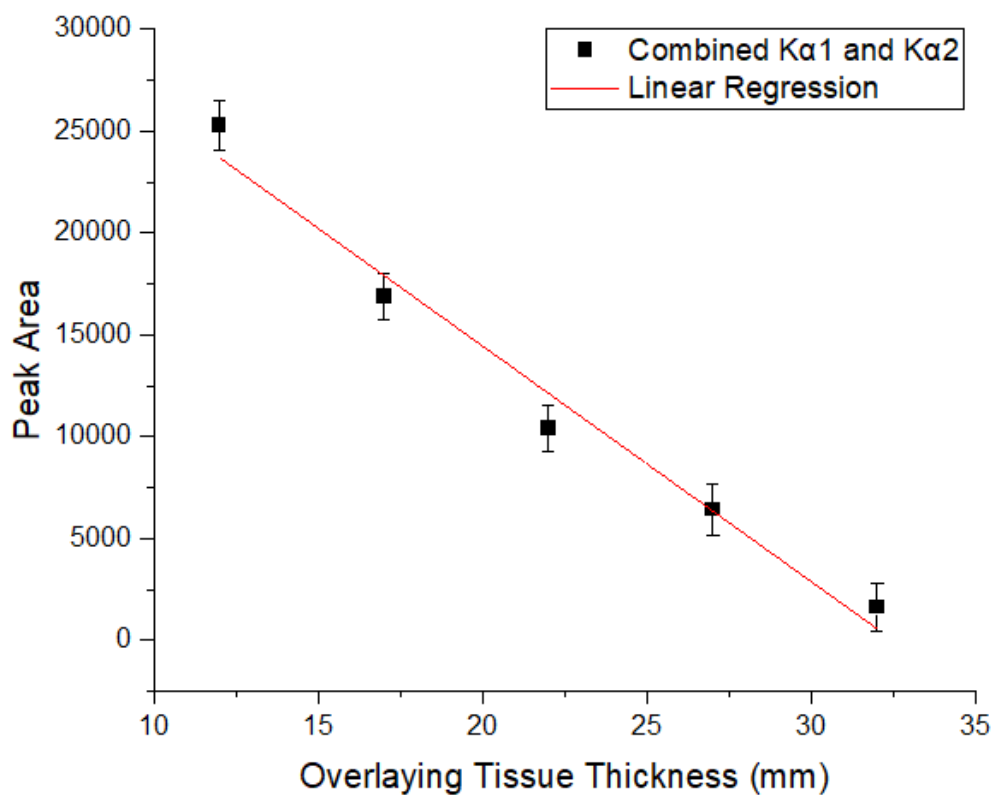


Figure 4.4: Peak area as a function of the overlying tissue thickness for the MDL calculation. It was fit with a linear regression analysis in red and the black is the combined Gd $K\alpha_1$ and $K\alpha_2$ with error bars. This is the plot for the four combined detectors.

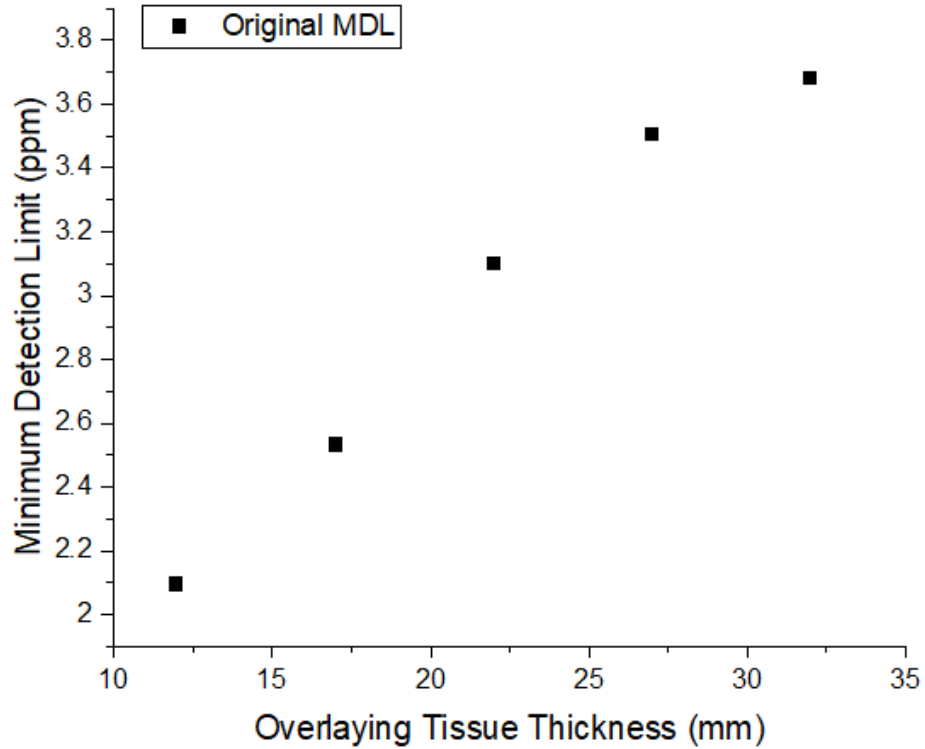


Figure 4.5: Natural logarithmic MDL as a function of tissue thickness for the liver phantoms. The black is the combined Gd peaks $K\alpha_1$ and $K\alpha_2$, it is the original MDL with no adjustments. These are the data from the four combined detectors.

4.0.4 Kidney Phantoms

The kidney experiment is similar to the liver once again. The energy spectra were collected and analyzed to determine the Gd peak areas. The peak areas were plotted as a function of the known Gd concentration (Figure 4.6). They were fit with a linear regression and resulted in calibration lines for the

calculation of the MDL for the kidney. Table 4.3 lists the MDL per individual detector, they are then combined using the inverse variance weighted mean. The fits for the Gd peaks have an average chi-square of 1.22 ranging from 0.84 to 1.88. This indicates that the mathematical model used to fit the data is relatively good. The MDL for the kidney calculated for this experiment is based off the 5 ppm data, calculating to 3.87 ppm.

Detectors	Minimum Detection Limit (MDL) (ppm)
D1	23.42
D2	7.71
D3	6.53
D4	6.36

Table 4.3: MDL per detector in ppm for the kidney. Detector one has the worse MDL since it has the worse energy resolution of all detectors.

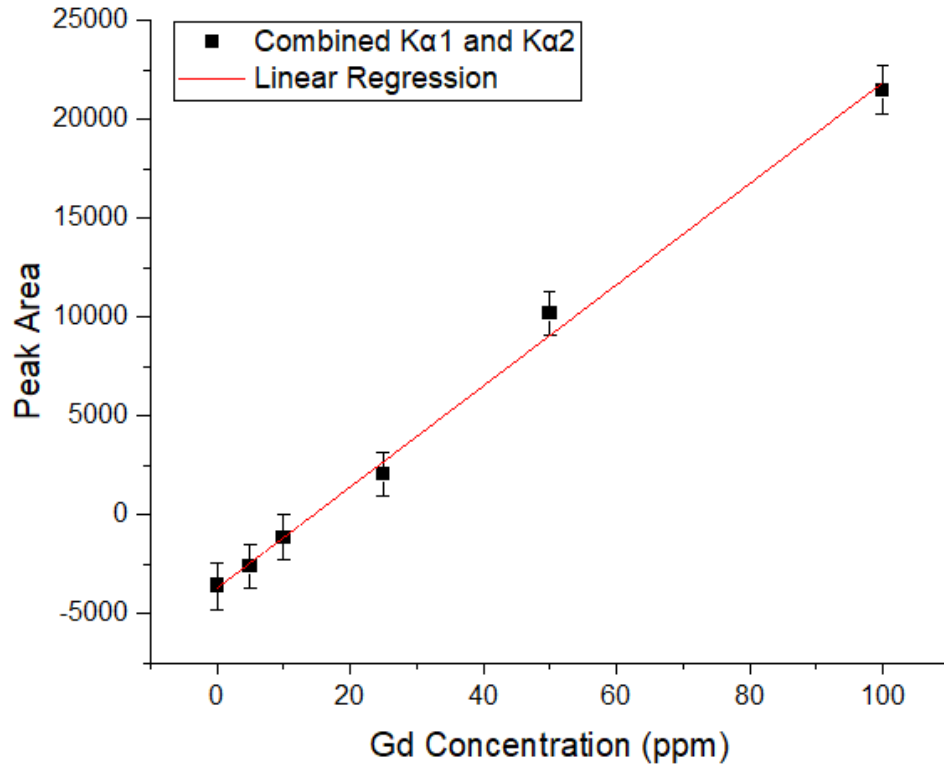


Figure 4.6: Calibration line for the four combined detectors. The measured Gd peak area as a function of the known Gd phantom concentrations for the kidney phantoms. It was measured at 11 ± 0.5 mm from the Cd-109 source for a duration of 30 minutes. The black is the combined $K\alpha_1$ and $K\alpha_2$ peak areas with error bars, fit with a red linear regression. This line has an R-squared value of 0.99.

4.0.5 Overlaying Tissue Thickness Kidney Phantoms

The detection of Gd in the kidney was observed for varying tissue thicknesses as well. The MDL was calculated for varying thicknesses at 11 ± 0.5 mm, 16 ± 0.5 mm, 21 ± 0.5 mm, 26 ± 0.5 mm, and 31 ± 0.5 mm. The 100 ppm phantom was chosen for the experiments due to the visibility of the Gd peaks. The peak area was plotted as a function of the overlaying tissue thickness (Figure 4.7). This resulted in an exponential fit analysis, instead of the linear analysis found from the liver phantoms. The values were then converted with the natural logarithm to have a more linear fit and have a linear analysis fit incorporated on the data. Therefore, the natural logarithm of the MDL was taken. The MDLs were plotted as a function of tissue thickness, Figure 4.8. As the thickness increases, the MDL also increases due to the increase in attenuation.

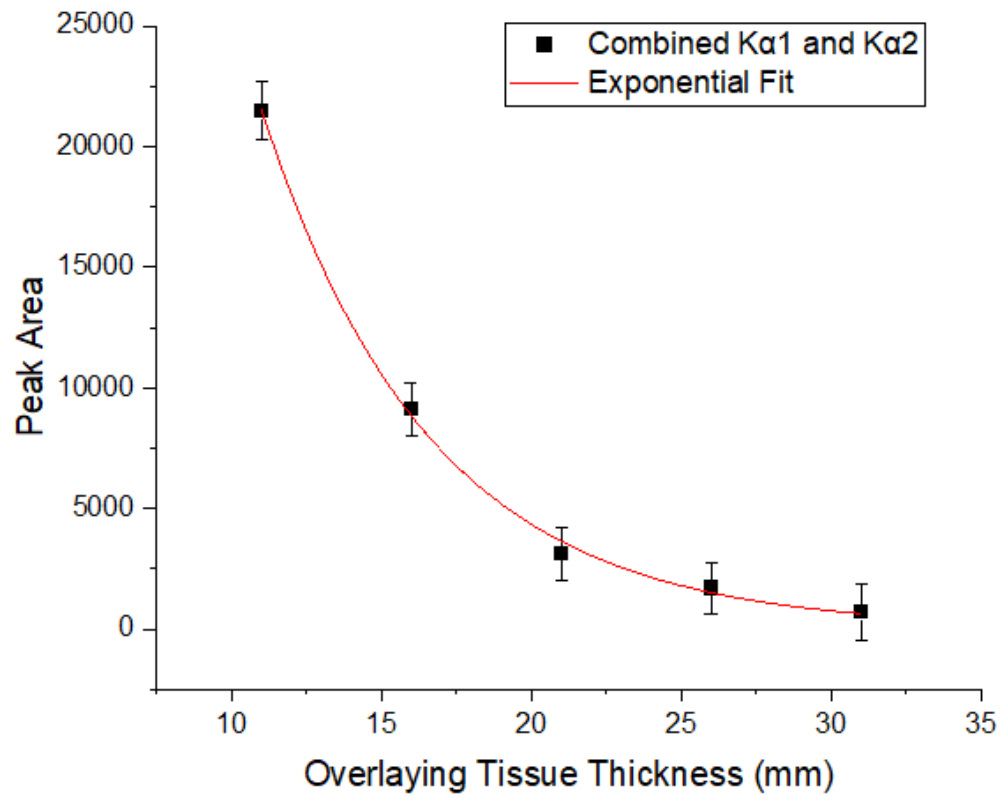


Figure 4.7: Peak area as a function of the overlaying tissue thickness for the MDL calculation. The black is the combined K α 1 and K α 2 Gd peaks, with error bars, fit with a red exponential fit. This is the plot for the four combined detectors.

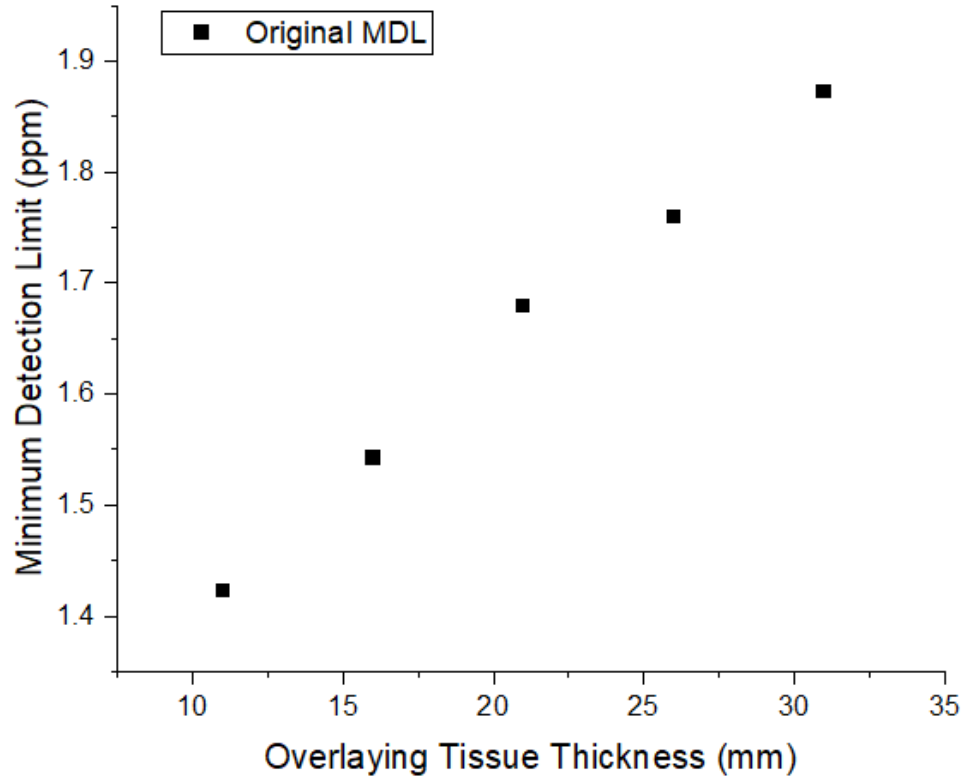


Figure 4.8: The natural logarithmic MDL plotted as a function of the overlaying tissue thickness. The black is the original MDL. This is the MDL plot for the four combined detectors.

4.0.6 Comparing Live Time with Real Time

Something that was quite interesting to see is that the live time of the detection system was very short compared to the real time when doing the 30-minute real time experiments. I wanted to look at the difference between the peak areas if I set the live time as 30 minutes instead of the real time. This resulted in the same peak areas as the 5-hour measurements, with a live

time of 30 minutes and a real time varying around 2 hours. One experiment was conducted with this type of time change. This was for the liver phantom of 100 ppm, sitting at a distance of 12 ± 0.5 mm. Taking the data from the third detector, the peak area was $133\,520 \pm 2610.6$, the other detectors have similar data. The peak area for the third detector for the 5-hour experiment was $128\,710 \pm 2770.5$ sitting at a distance of 6 ± 0.5 mm. This shows that the new source would not be the most optimal choice for the clinical setting since humans would be quite uncomfortable sitting in front of a detector for approximately 2 hours. A source with an activity between the old and new source may be realistic clinically.

Chapter 5

Discussion

The activity of the source was 0.78 GBq when I first started the thesis experiments. As the 88 keV photons only occur in 3.7 % of decays, this is not a very strong fluorescing source. In order to improve the relative uncertainty $\frac{1}{\sqrt{N}}$, where N is the number of counts and \sqrt{N} is the Poisson uncertainty, the counting time was elongated, beyond that which would be possible for a patient. This improved the MDL and by adjusting, the MDL could be predicted for a 30-minute measurement with a stronger source of 5 GBq. The time adjustment, as mentioned above, has a relationship of $\text{MDL} \propto \frac{1}{\sqrt{t}}$, to scale the time for a 30-minute measurement instead of 5 hours. The activity relationship is $\text{MDL} \propto \sqrt{\frac{A_0}{A}}$, where A is the 5 GBq and A_0 is the 0.78 GBq source. The dead time was large since the big water phantom was scattering photons and emitting a large background signal. This increased the dead time and it varied around 20 % for each measurement. Therefore, the dead

time adjustments could not be completed. Increasing the concentration of Gd in the phantom increased the Gd peak area, which was expected as the interactions with Gd would also increase. From these Gd signals, a calibration line of Gd peak signal versus concentration was created which helped with the calculation of MDL.

The liver phantom MDL was slightly larger than the measured kidney MDL due to the larger size of the phantom. The liver's Gd concentration was spread through a 2 L volume compared to the kidney phantom that had the Gd concentration focused in 125 ml in front of the face of the detector, making it easier to detect.

For the overlaying tissue experiment, the MDL increased as the tissue thickness increased. The relationship was exponential and converted with the natural logarithm to observe a more linear relationship. The increase in MDL is due to two main factors, both resulting from the Gd phantom moving further away from the source-detector. One is a geometrical factor, explained in further details below. The other factor is where both the 88 keV gamma-rays and emitted Gd x-rays are being attenuated through the intervening water. The best measurements were found to be at 6 ± 0.5 mm from the source. The MDL for the liver is $3.68 \mu\text{g Gd/g}$ and the kidney MDL is $4.26 \mu\text{g Gd/g}$. The MDLs are slightly larger than the measured MDLs coming from Lord, M., et al., (2017). They had a measured MDL of $1.64 \mu\text{g Gd/g}$ plaster, for the tibia. They did not have the water phantom causing more attenuation interactions, which would explain why my values

are larger. This would suggest that the liver could be measured with the K-XRF method, but the patient has to be in the low to normal BMI range and would have to have a significant amount of Gd for optimal detection.

The kidney phantom was similar to the liver phantom but was much smaller. The source activity was slightly lower due to the decay time of the experiments. The MDL was from three data sets 5 ppm, 10 ppm, and 25 ppm, compared to the liver which only came from the 5 ppm data set. This gave an overall better calculated MDL at $4.26 \mu\text{g Gd/g}$. Figure 3.5 above shows an exponential relationship between peak area and overlaying tissue thickness which was interesting compared to the more linear relationship observed with the liver phantom. This could be due to the small size of the kidney, as the tissue thickness increased, the MDL increased. This means the large torso water phantom has more interactions than the kidney phantom and the detection of Gd dropped exponentially. Therefore, Gd in the kidneys would be quite difficult to detect with patients that are in the high BMI category.

A published study compared the urine Gd concentration relationship with the detection of Gd in bone, and there was no significant relationship between the two, suggesting an alternative storage site such as the kidney might be storing the Gd in the medulla or the cortex of the organ. The Gd could also be coming from other storage sites, which is why the liver was examined as well. The liver has a lower MDL of $3.68 \mu\text{g Gd/g}$ compared to the kidney at $4.26 \mu\text{g Gd/g}$. When comparing the much smaller mass of the kidney

compared to the liver, the very similar MDL means that for the kidney, most of the Gd is within the field of view of the detector, compared to the liver, where most of the Gd is further away from the field of view since it is spread within 2 L. This topic will be further discussed below.

5.0.1 Comparing MDLs Between the Liver and Kidney

The liver is a lot larger than the kidney. Expressing the MDL in terms of mass gives a different perspective. The liver phantom has a volume of 2.175 L and an MDL of 3.68 ppm, in terms of mass that is 8.0 mg. Compared to the kidney phantom, which has a volume of 125 ml and an MDL of 4.26 ppm. In terms of mass, the kidney MDL is 0.532 mg. That is quite a substantial difference in MDL. The liver phantom extends outside of the range where the source-detector system is efficient. Since the size of the detectors are quite small, even with adding the three other detectors making it into a cloverleaf formation, the detection efficiency is not optimized for a large phantom. For the best optimal detection efficiency, it is reliant on the radiation interactions and the size of the detectors. If they were large enough they would detect 100 % of the particles incident on the detector, although this is impossible for this scenario. As proved by Ranger, N. (1999), there is a strong correlation between the source-to-detector distance and the geometric efficiency. Radiation is emitted isotropically, if the source is close to the geometry then only a small fraction of the events impinge upon the detector. In another sense, the geometric efficiency of the detectors decreases

when the source-to-detector distance increases. This would be the definition of the inverse square law [22]. The intensity (I) of the radiation is inversely proportional to the distance (d^2) from the source ($I = \frac{1}{d^2}$).

5.0.2 Comparing Gd Levels with Other Research

A study explored by McDonald, R. et al, observed the deposition of Gd in the tissue of 20 rats. They received intravenously 2.5 mmolGd/kg over a 26 days period. The study looked at the distribution 7 days after injections with the ICP-MS method. The kidneys had a concentration between 49.5 - 2179.7 μg Gd/g tissue, and the liver between 8.9 - 511.6 μg Gd/g [16]. The two organs had significant levels of Gd once the Gd treatments were finished. The kidneys especially had a large concentration due to its function of filtration. The MDL from our detection system starts at 4.26 μg Gd/g therefore detection at this level would be possible. As for the liver, they found it to have low values. The liver MDL here is lower, however, than the lowest concentration from their study, therefore detection may also be possible if using the K-XRF HPGe Cloverleaf detection system.

Another study looked at the Gd concentration in the kidneys and liver of rats that have been exposed to doses of GBCAs. Twenty-eight days after the Gd administration, there was no Gd found in the livers using ICP-MS. There was however a large concentration found in the kidneys between 25 nmol/g and 204 nmol/kg [1]. Comparing these results to the MDL of this detection system for kidney, the 25 nmol/g converted into units of μg Gd/g,

is only at $3.93 \mu\text{g Gd/g}$. The detection of Gd in the kidneys at these levels might not be possible due to the higher MDL. There is insignificant research for liver and kidney Gd levels found from human research. More research in increasing the sensitivity of the detection system is recommended.

5.0.3 Dead Time Configuration

Dead time is defined as the summation of all the processing times of the different components in a detection system, this includes the detectors, the amplifiers, the preamplifiers, and so on. There are two models for dead time, the paralyzable and non-paralyzable. The non-paralyzable model is a fixed dead time where events occur during the live period of the detector and the events that occur during the dead period are not recorded and do not affect the system. This compares to the paralyzable model, where the fixed dead time follows the events during the live period of the detector, but the events that occur during the dead period create another fixed dead time. This can result in lost events. If the counting rate is high, therefore, as when we have a high activity radioactive source implemented into a clinical setting, then the system might turn off or stop recording pulses since the pulses and dead times are overlapping and do not record events. The dead time of a general radiation system should be set as less than 20 % [2]. The experiments conducted in this thesis had a dead time that varied around 18 %. Having a high activity source of 5 GBq would increase the scattering with the water phantom, increasing the dead time significantly. Certain

changes to the detection system would have to be implemented to decrease the dead time. With a new source, we might consider changing the source-to-detector distance. We would have to try to find the optimal position where the detectors do not become saturated as well as not worsening the resolution too much. Another concept to keep in mind is changing the rise and flat top times of the pulse shape and timing properties. The time resolution depends on the average rise time and the change in the pulse shape from one event to the next. If the rise time is set at a short time, the dead time will then be less, but the energy resolution will get worse. Therefore, an optimal rise and flat top time has to be found to lower the detection limit [2].

5.0.4 Comparison of Neutron Activation Analysis vs. K-XRF

As mentioned in the Introduction section, there is another method of Gd detection, using prompt gamma neutron activation analysis. It is a method previously used in our laboratory by Grafe, J. L. in 2012. It is a non-invasive method of detection by using neutron activation. The neutron capture cross section for $Gd-157(n,\gamma) Gd-158$ is used and is based on the 254 000 b thermal neutron capture reaction. Gd-157 emits gamma-rays promptly, therefore the irradiation and counting of gamma-rays is taken at the same time. This is similar to the XRF system used in this thesis. Since Gd has a large cross section, it is optimal for neutron activation. The activation study observed

two gamma-ray energies, 79.5 and 181.9 keV, following the neutron capture. They also observed the kidney and liver using a similar approach with the water torso phantom and the cylindrical kidney phantom of 125 ml and liver phantom 2 L. The MDL for kidney at 79.5 keV is 19 ± 2 ppm or 2.3 ± 0.2 mg and at 181.9 keV is 7.8 ± 0.4 ppm or 0.97 ± 0.05 mg [4]. When comparing this MDL to the experimental MDL from K-XRF HPGe detection system, they are poorer. The MDL from this thesis is 4.26 ppm or 0.532 mg. The K-XRF detection system is more reliable when it comes to detecting lower levels of Gd compared to the neutron activation method. The higher MDL for the neutron method might be due to the proximity of the kidney to the detector, neutron shielding and collimating apparatus, causing a higher background in the kidney spectrum. Whereas the K-XRF detection system, the size of the kidney is more beneficial since the Gd is in the field of view of the source and therefore, has optimal detection of Gd.

The neutron activation system had a similar MDL for liver compared to the K-XRF method. The MDL for liver for the neutron detection system was 7.1 ± 0.4 ppm for 79.5 keV and 3.3 ± 0.1 ppm for 181.9 keV. This compares to the K-XRF detection system with an MDL of 3.68 ppm for the liver. The two detection systems are similar, therefore the choice of method of detection may be up to preferences or availability rather than better detection. Another assumption is that the prompt gamma neutron activation system has a wider volume of interest compared to the K-XRF detection system. The neutron activation system, therefore, considers the entire liver where the K-XRF can

only measure part of the liver that is sitting in front of the face of the detector.

5.0.5 High Activity Source

The experiments with the weaker source were altered to conform to those anticipated in a clinical setting with a strong radioactive source of 5 GBq. The new source has the activity of 5 GBq and the experiments were measured at a real time of 30 minutes to compare to the experiments with the weaker source. The source was very strong, therefore, the source-to-detector distance had to be optimized before starting the experiments. As seen in the Results Section – Source-Detector Distance, the distance had to be found by placing an object in front of the source, in this case the bottle of Omniscan, to produce a visible signal that the peaks could be analyzed. The optimal dead time would be anything under 40 % since previous researchers had found that the dead time correction algorithm is less accurate at higher dead times. However, since the distance for a 40 % dead time with this new source was making it difficult to see the Gd peaks, this dead time was not realistic. Therefore, the object was placed in front of the detector face in the water phantom and a large dead time of around 70 % was accepted. The goal was to find a distance where the detectors were not getting saturated with counts, where the energy spectrum was not distorted, and for the peak analysis fit to have a reasonable fit on the Gd peaks. Therefore, the distance of 10 ± 0.5 mm from the detector face was the best distance. There is an added millimeter to this distance due to the thickness of the water phantom and

thickness of the bottled phantoms. Therefore, the distance of 11 ± 0.5 mm was chosen for the optimal source-to-detector distance. The fact that the combination of detectors and electronics seem able to operate effectively and accurately in this experiment at a very high dead time of around 70 % is notable.

5.0.6 Comparing Liver vs. Kidney

The liver again is much larger than the kidney. The liver has a volume of 2.175 L with an MDL of 3.61 ppm. In terms of mass, this means the liver is 7.8 mg. Compared to the kidney which is a volume of 125 ml and has an MDL of 3.87 ppm, in terms of mass, this is calculated to be 0.48 mg. There is quite a substantial difference in MDL, when comparing them in units of mass. This difference probably reflects the smaller size of the kidney being in a much more measurement efficient geometry than the larger liver, much of which would be inefficiently sampled.

5.0.7 Comparing the Two Sources

The old and new source experiments are quite comparable where the kidney and liver MDLs are similar when using the adjusted MDL from the initial experiment with the weaker source. The MDL for kidney was 0.532 mg with the weaker source and is 0.48 mg with the new source. They have a difference of 0.052 mg. They are comparable, the difference is the source was

much stronger and more particles were incident on the detector increasing the amount of counts. This lowered the MDL for the kidney. Whereas the liver MDL for the weaker source was 8 mg, and with the new source is 7.8 mg. They only have a small difference of 0.2 mg and can therefore be approximately equivalent. The difference could again be the increase of events incident on the detectors. If we were to compare to the original MDLs from the weaker source, there is quite a difference. The MDLs are slightly better in terms of the new source, which had a running time of 30 minutes to match a better human clinical setting. Optimizing the detector capabilities in terms of geometry, detector efficiencies, and dead time would improve this detection system. Overall, it was encouraging to observe that the results with the strong source were as good as they were despite both having to increase the source to phantom distance and the high dead time.

Chapter 6

MCNP Simulations

Monte Carlo N-Particle (MCNP) is a coding software that can be used to predict the tracks of many particle types over broad ranges of possible energies. The code uses the generation of random numbers to make choices of interaction, and because this is rather like rolling a ball on a roulette wheel, it is known as Monte Carlo radiation-transport. The MCNP 6 code can handle both neutral and charged particles, x- and γ -, and includes various physics models for energies above cross-section table ranges, material burnup features, and delayed particle production. MCNP allows the user to input geometric specifications, a description of materials and cross-sections, the location and particle-type of sources and the type of answers or tallies desired [20]. The main input file contains the information to describe the problem. It uses units in centimeters (cm) for length, energy is in MeV, the mass density is in grams per cubic centimeter (g/cm^3), and atomic density is

in atoms/barn-cm. The code is composed of cell cards which are defined by assigned surfaces bounding to “the cell”. The cell is essentially a volume of a known material of a specific density within a region defined by the surfaces. The shape of cells can be complex as MCNP allows a range of surfaces to be defined using planes, cylinders and spheres with locations defined against the x-, y-, z- axes [20]. The user can specify materials as single elements or mixtures of elements, choose particle types and physics models and define source type, shape, and emission angle. Users must decide a tally specification. The tally is very important for determining the product that will be shown in the output file. They specify what the user wants from the Monte Carlo simulation, for example, the current across the surface, the flux at a point and so on [20].

The most recent release MCNP6 was used for the simulations. It was first introduced by Los Alamos laboratories in 2013. MCNP6 has a few new added features related to this thesis work, such as the new enhanced photon form factors and complete atomic relaxation processes [20]. It can represent coherent and incoherent events properly for back-scattering experiments.

The MCNP code is used in this thesis to model the experimental results for the detection of Gd using a simulated K-XRF HPGe cloverleaf detection system. The MCNP geometry of the kidney detection system is shown in 6.1. It is composed of the Cd-109 source, the two phantoms (torso and liver/kidney), the source, and the four HPGe detectors. The simulations are very similar to the experimental method, where the Cd-109 source is placed

in front of the face of the detectors and emits 88 keV gamma-rays. In the experiment, the source is in a collimator which only allows photons to be emitted in the direction of the phantom. In the MCNP model, the source is a point source directed in a single forward direction. The gamma-rays in the model interact with the phantoms simulating several concentrations of Gd in the liver and kidney. The Gd in the phantoms will then emit Gd x-rays and the two x-ray peak areas ($K\alpha_1$ and $K\alpha_2$) that I am interested in will be extracted from the overall MCNP energy spectrum. The tally chosen for the simulations in my case is the F8 tally, where the output is the energy distribution of pulses created in a detector. The dimensions of the phantoms as well as the irradiation and detection system are matched to the experimental method. Each detector had its own energy spectrum similar within uncertainties to the experimental method.

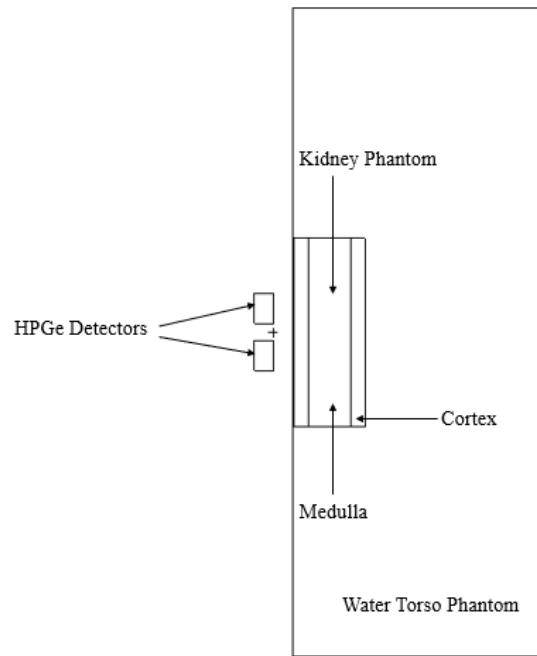


Figure 6.1: MCNP geometry of the detection system with the cortical kidney phantom inside the torso phantom.

For the peak area analysis, the two Gd peaks at 42.308 and 42.996 keV were found from the MCNP energy spectra data source. The background signal was subtracted from the Gd x-ray peak areas. The signal from the two Gd $K\alpha$ x-ray peaks were combined, similar to the experimental method.

Chapter 7

MCNP Results & Discussion

7.0.1 Kidney Simulations

The initial kidney simulations were to directly compare to the experimental results. This allowed me to check whether the code was accurately predicting the experiment. It is an extremely difficult and long task to create MCNP simulations where the peak areas can be directly compared to experiment. For example, the exact locations of crystals inside the can, the dead surface layers of the detector, and the exact construction of the source and collimator are required to be known. Therefore, the data were normalized to the 100 ppm phantom in each case to be able to compare easily with the experimental data. A few simulations were performed with varying concentrations of 0 ppm, 5 ppm, 10 ppm, 25 ppm, 50 ppm, 100 ppm, and 200 ppm (Figure 7.1). The data followed a similar trend to the experimental data but the axes in the MCNP calibration chart are of Gd x-ray per emitted source photon.

Normalizing the data sets for the simulations and the experiments was the best choice for comparing the two (Figure 7.2).

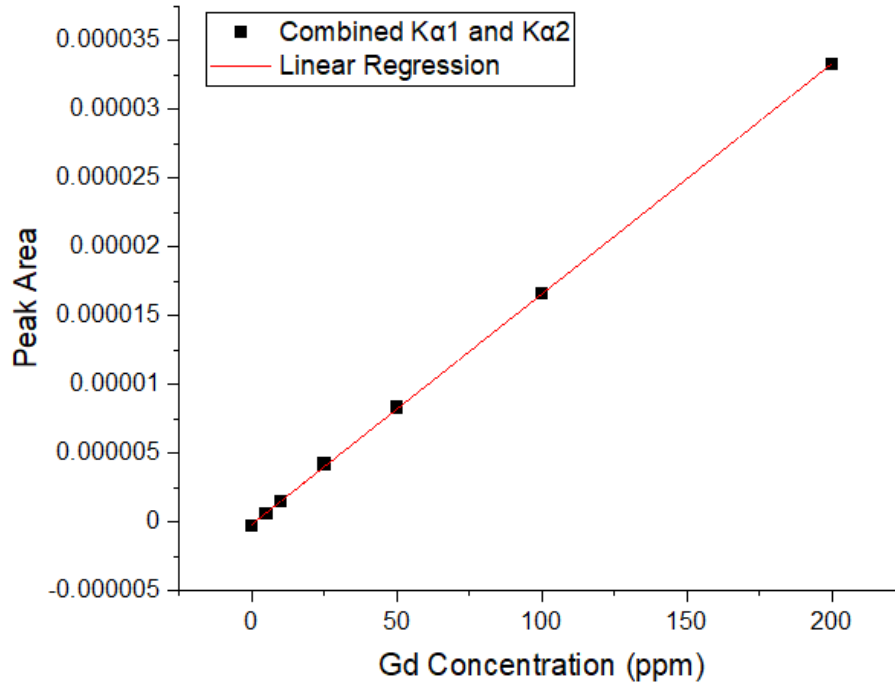


Figure 7.1: Calibration line for the four combined detectors. Where the peak area per emitted source photon is plotted as a function of the Gd concentration for the MCNP simulated data. The black is the combined $K\alpha_1$ and $K\alpha_2$ Gd peaks fitted with the red linear regression.

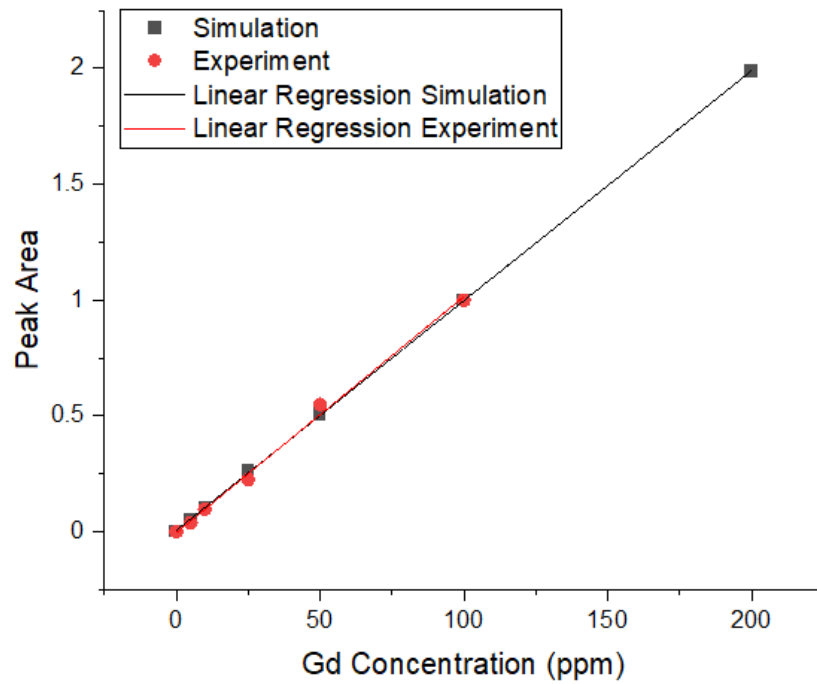


Figure 7.2: Normalization plot for the four combined detectors, comparing the experimental and simulated data. The grey line is the simulated data fit with a linear regression. The red is the experimental results fit with a linear regression. The intercept is at 0 since the data is normalized to 1 at the 100 ppm phantom.

In Figure 7.2, the data sets are very similar to each other. They both follow a linear relationship with slopes that are the same to within uncertainties. The slope for the four combined detectors for the simulation is 0.0099 ± 0.00004 and the slope for the experiment is 0.0102 ± 0.00031 . Therefore, there is no significant difference between the two slopes ($-3.0 \times 10^{-4} \pm -2.7 \times 10^{-4}$), suggesting the simulation is accurately modelling the experiment and can be used to make predictions in this thesis work.

7.0.2 Liver Simulations

The liver phantom simulation was similar to the kidney. The phantom was placed at the wall of the torso phantom and placed in front of the face of the detectors and source assembly. The phantom concentration varied at 0 ppm, 4 ppm, 12 ppm, 25 ppm, 50 ppm, and 100 ppm for the experiment. The simulation for the liver had similar concentrations to the kidney varying at 0 ppm, 5 ppm, 10 ppm, 25 ppm, 50 ppm, 100 ppm and 200 ppm. One phantom with a larger concentration was added to the MCNP simulations as it helped in the development of the peak extraction method. The peak areas were plotted as a function of the Gd concentration in Figure 7.3. The data increases as the concentration increases, in a linear relationship. The simulation and experimental results were again normalized to the 100 ppm phantom for better comparison in Figure 7.4.

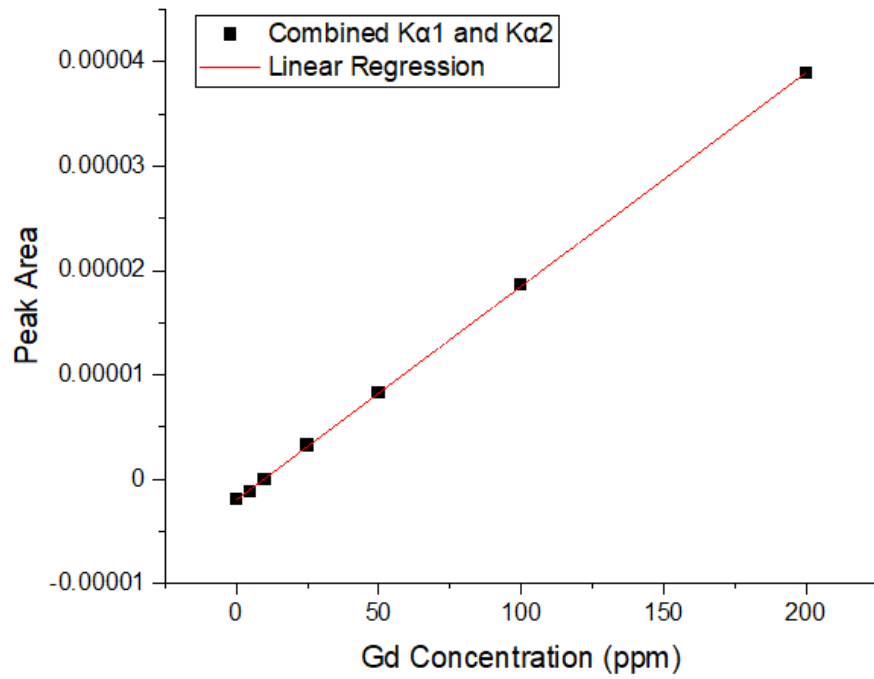


Figure 7.3: Simulated data for the four combined detectors, showing the peak area as a function of Gd concentration. The black is the combined Gd K α 1 and K α 2 peak areas and the red is the linear fit. The intercept is negative due to the background being subtracted from the peak areas.

Figure 7.4 displays the differences between the two data sets, simulation and experiment, respectively. The slope for the four combined detectors simulation is 0.00997 ± 0.00005 , and for the experiment it is 0.00976 ± 0.00038 . These slopes are the same to within uncertainties (simulation minus experiment = $2.10 \times 10^{-4} \pm -3.3 \times 10^{-4}$) which again suggests the simulation is a good model of the experiments and could be used for further research purposes.

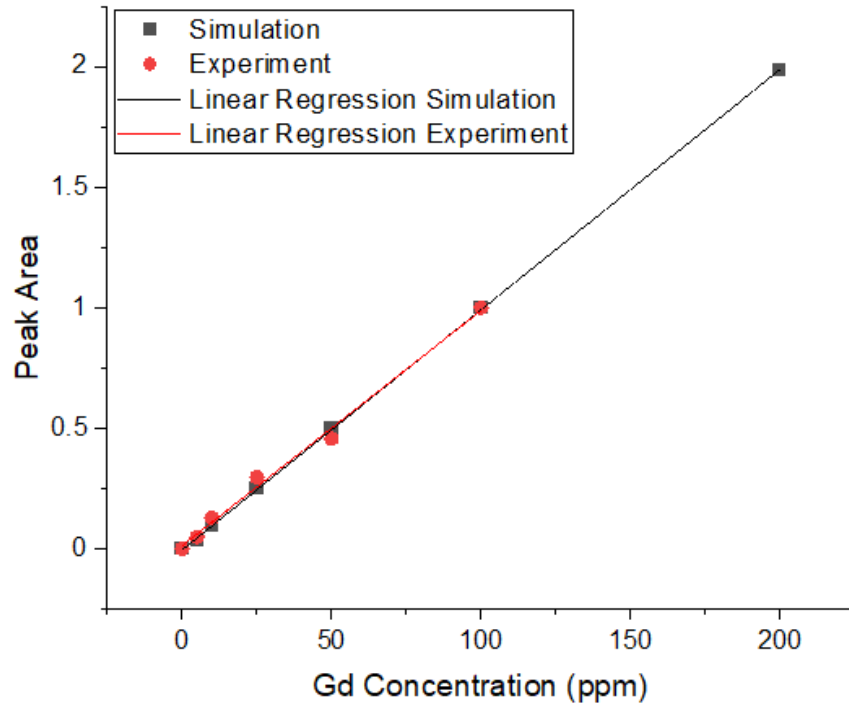


Figure 7.4: Normalization data for the four combined detectors, where the peak area for the simulation and the experiment are plotted as a function of the Gd concentration. The grey are the simulated normalized data with a linear fit. The red are the experimental normalized data fit with a red linear regression.

7.0.3 Cortical Kidney Simulations

The purpose of MCNP is to observe and predict things that either cannot be measured or are too costly, or time consuming experimentally. Which is why the kidney was simulated a second time but with varying cortex and medulla concentrations. The kidney's cortex is near the wall of the kidney and the medulla is in the center. Since the kidney can be separated in two compartments (cortex and medulla), it would be interesting to see how variations in Gd distribution between the cortex or the medulla would affect the accuracy of experimental estimate of kidney Gd. Some published data have observed that there is more Gd in the cortex of the kidney, around 1.5 times higher than in the medulla. Therefore, this was simulated in MCNP. The cortical kidney concentrations were calculated as the average concentration that could be estimated by MCNP, they varied at 0 ppm, 3.66 ppm, 8.71 ppm, 22.31 ppm, 43.32 ppm, and 87.57 ppm. The peak areas were plotted as a function of the Gd concentrations in the cortex/medulla (Figure 7.5).

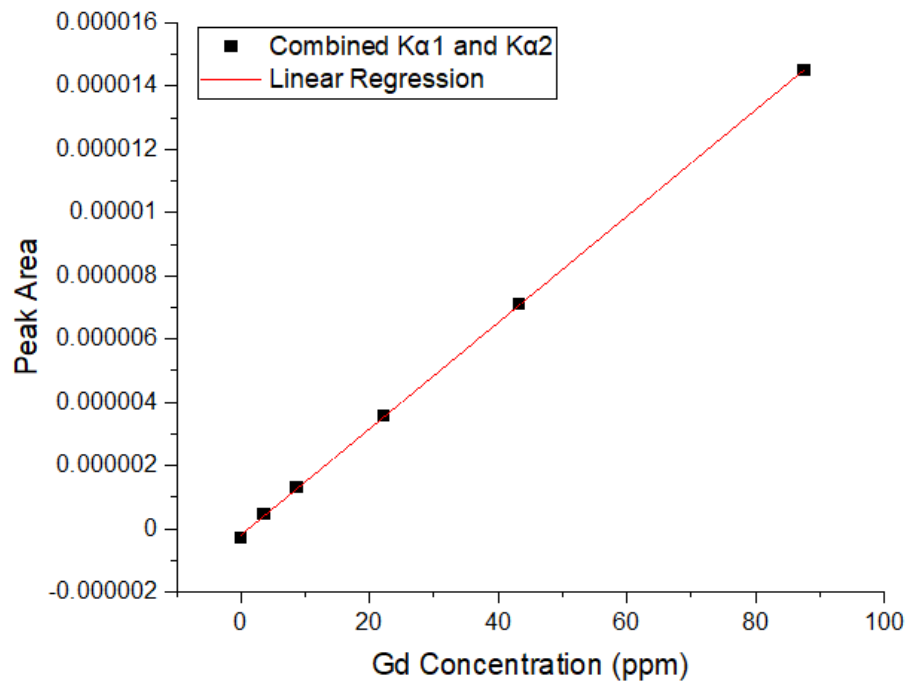


Figure 7.5: Peak area as a function of Gd concentration for the four combined detectors. Where the cortex and medulla have different concentrations. The combined $K\alpha_1$ and $K\alpha_2$ of Gd is in black and is fit with a linear regression. The slope for the linear fit is $1.679 \times 10^{-7} \pm 6.835 \times 10^{-10}$.

To further make sure that experimental estimates would be correct even if the Gd was heterogeneously distributed, two simulations grossly varying the concentration of the medulla and the cortex were run. The peak area, detectors, and concentrations are observed in the table below (Table 7.1). Using these peak areas and the calibration line shown in Figure 7.1, the average concentration in these modelled kidneys could be estimated. These could then be compared to the values input to the MCNP code. The MCNP model predicts average values of 159.9 ± 3.3 ppm and 140.9 ± 2.4 ppm. The corresponding input values are 163.7 ppm and 136.3 ppm. Even with grossly abnormal variation in Gd kidney distribution, the MCNP model suggests that experimental results will be accurate to within 5% of the true value.

Detectors	a) Peak Areas: Medulla 100ppm, Cortex 200ppm	b) Peak Areas: Medulla 200ppm, Cortex 100ppm	Ratio a) / b)
D1	2.138×10^{-5}	1.861×10^{-5}	1.148
D2	2.915×10^{-5}	2.530×10^{-5}	1.152
D3	2.682×10^{-5}	2.398×10^{-5}	1.096
D4	2.899×10^{-5}	2.580×10^{-5}	1.124

Table 7.1: Opposite Gd concentrations for the medulla and cortex of the kidney peak areas, for each detector.

The mean ratio for simulation a)/simulation b) is 1.130 ± 0.026 . Therefore, this is a consistent and statistically significant difference. There is a clear disproportionate effect of the distribution of Gd, with the Gd that is in the cortex near the source-detector assembly contributing to the detection

much more efficiently than the rest of the kidney. This is observed with the calculation of the total mass of Gd in each phantom model above a) and b). The total mass of Gd in phantom a) is 18.9 mg. The total mass of Gd in the phantom b) is 15.8 mg. The simulation a) gives 1.13 times the number of counts as simulation b) and has 1.19 times more Gd.

Chapter 8

Conclusion

This thesis work involved the application of a K-XRF detection system previously used in bone-Gd measurements, to detection of Gd in liver and kidneys for future detection of Gd in individuals who have received GBCAs. It looked at a series of phantom measurements and considered interpatient variability to determine the feasibility for human measurements.

The MDL was determined by this thesis work for both organs to demonstrate if *in vivo* measurements would be feasible. The Thesis concludes that the detection system can measure low Gd concentrations. The possible Gd storage sites of the liver and kidneys could be observed, using this detection system.

8.0.1 Moving Forward

The detection of Gd in the liver and kidney has been successful with phantoms. The next steps would be implementing the detection system for *in vivo* measurements in humans. This poses many questions for radiation safety. Before directing a radioactive source at the torso of human beings, the dose to the surrounding organs must be observed. Therefore, I would suggest measuring the radiation dose to surrounding organs that are in proximity to the organs of interest. The organs at risk (OAR) when irradiating the liver region would be the right lung, potentially the heart, the stomach, the pancreas, and the duodenum. Placing thermoluminescent dosimeters (TLDs) around the liver phantom during measurements and reading the TLD dose information after irradiating for the expected duration of a clinical measurement, would give a better idea of the OAR. This would also have to be conducted for the kidney, where the OARs for kidney, from the back of the human body would be some ribs, the lungs, potentially the heart, the liver, the stomach, the pancreas, and the large intestine. The dose to the organs is expected to be small, but we have to follow the rules of ALARA (As Low As Reasonably Achievable). Knowing the dose to the surrounding areas is crucial information in the assessment of the risks of the measurement.

8.0.2 Clinical Studies

Once the OARs have been determined, the next steps would be to start clinical studies. First measurements of the MDL (which would allow improvement of the K-XRF detection system) should be performed with *in vivo* measurements of humans that have previously received GBCAs. Lord, M et al, have already performed some clinical studies for the tibia. I would like to improve upon her methods for the clinical studies by recruiting a larger population size compared to her study. Better medical data on the patients, knowing the brand of GBCAs and dose would also be an improvement. A larger population with fewer uncontrolled variables would be required for the data to be significant and to make a meaningful conclusion.

The next set of observations would be to compare the different GBCA brands and doses with the liver and kidney data from humans. There are important data from animal studies that have shown storage in these organs of interests for specific brands of GBCA; this would be interesting to see for *in vivo* measurements in humans as well.

8.0.3 Detector Capabilities

The MDL could be lowered for better *in vivo* measurements of Gd in the liver and kidney. For the MDL to be lowered, the possible count rate in the detector would need to be increased to detect more Gd x-rays. As mentioned in the discussion section, with the current system if the count rate is

increased, the dead time would also increase. Therefore, there would need to be some count rate optimization process for a better MDL. One that is currently under development is the improvement of pulse restoration electronics. As mentioned above, pulse pile-up is a concern that arises and contributes to the high MDL. To lower the MDL, pulse pile-up would have to be reduced. Pulse pile-up is when multiple radiation events arrive within the live time of the detector. The detector does not have enough time to fully recover from the primary events, and to return to baseline before the subsequent radiation events arise. The pulses add together and are recorded as a single higher energy pulse. This creates background and can remove signal. A new method has been implemented for real-time decoding of pulse pile-up events. It is a model-based signal-processing algorithm that can accurately determine the number, time-of-arrival, and energy of each event from the detector output [24].

This new digital pulse processing system uses a non-linear, model-based, real-time, signal-processing algorithm. Where the output of the radiation detector is characterized by the algorithm using the equation below:

$$y[n] = \sum_{i=1}^N \alpha_i h[n - \tau_i] + w[n] \quad i = 1, 2, 3, \dots, N \quad (8.1)$$

Where the digitised radiation detector time series ($y[n]$) is modeled as the sum of an unknown number of radiation events (N), that has a random time of arrival (τ_i), and amplitudes (α_i), that are interacting with the

detector. The radiation detector has an expected pulse shape ($h[n]$) with a noise process ($w[n]$). The pulse pile-up algorithm starts from the digitised output of the detector using an analogue to digital converter. The first step is to characterize the detector, so the detector time series is the input, it determines the pulse-shape response of the detector. It is constructed by doing the average of the large number of individual radiation events. The next step is the event localisation, to find the number of time-of-arrival of each event from the data.

Next is the pulse identification stage, where the energies of the radiation events are determined from the data. The final step is the validation stage, where the parameters that were estimated from the equation above, are combined to reconstruct the model of the detector data. Results from this algorithm have shown a dead time staying consistent at less than 10 % with an increase of the input count rate, ranging from 50 000 counts/second to 150 000 counts/second. The Full-Width Half Maximum only degrades slightly, therefore the resolution at the high count rates stay slightly consistent. The current dead time with the new source is around 75 %, for real time measurements of 1 800 seconds, then the live time is only 450 seconds. If the dead time for the K-XRF detection system was reduced to 10 % by the new pulse processing, then the live time could go up to 1 620 seconds, therefore reducing the MDL by the square root of 450s/1620s, giving an MDL of 0.53. This decrease would improve the detection efficiency of the detector and would make it ideal for detecting Gd in humans in a clinical setting.

This method is currently undergoing investigation for implementation to the Cloverleaf detection system. It would decrease the dead time, keep resolution to stability with high count rates, allow real-time decoding of multiple events pulse pile-up instead of eliminating the missing data from the events, which would improve the detection system.

8.0.4 MCNP Simulations

The MCNP simulations were found to compare well to the experimental data thus suggesting that even the simple simulations were an accurate model of the liver and kidney phantom experiments. The simulations which varied the distribution of Gd in the kidney medulla and cortex were successful and determined that a Gd distribution between the cortex and the medulla does not affect the accuracy of the experimental estimate of kidney Gd. The XRF signal depends on average Gd concentration or total mass of Gd in the kidney.

It is extremely difficult to create MCNP simulations where the results can be directly compared to the experiment rather than normalizing the data. There are many factors that need to be exact and known, for example the locations of the crystals inside the can, the dead surface layers of the detector, and the exact construction of the source and collimators. A simplified version of the experiment was modelled with MCNP and improving the simulation code would therefore be the next step towards using the model as a predictive tool. The most important concept of the use of codes like MCNP is to

simulate an experiment that cannot be replicated in a laboratory due to other factors. Thus, having the specifications of the factors above would improve modelling and prediction.

The output from the MCNP simulation is of the F8 tally, where the energy distribution of pulses created in a detector is recorded. The peak areas are difficult to be extracted from this output file, therefore, better peak extraction should be implemented. Due to time restrictions, I was not able to use the proper coding tools for peak analysis. I suggest creating a code, in the language preferred by the user, that would specifically plot and calculate the peak areas, which should be user friendly, and which would be time efficient to use.

8.0.5 Conclusions

Gd is currently used for the better contrast of tumor imaging during an MRI. It is administered as a Gadolinium-Based Contrast Agent. There have been concerns for the safety of patients that have impaired kidney function. There is a patient advocacy group who are suggesting that there are patients showing subclinical signs similar to NSF, such as pain in the abdominal region, pain in their arms and legs, brain fog and painful skin thickening. This has led to extensive ongoing research of the retention of Gd in the body and there is a growing concern for the safety of GBCAs. The contrast agents are useful for tumor imaging but may also rarely cause symptoms of toxicity in some patients.

There are many organs that have been determined as storage sites for Gd, such as bone, liver, kidneys, and the brain. The detection of Gd in liver and kidneys using the K-XRF detection system has been successful. Clinical studies for *in vivo* measurements in humans are recommended to determine if these organs are actual storage sites of Gd. There is still the question of how the dissociation of Gd is undergoing through the body and where is it being stored?

This thesis has demonstrated successful Gd detection in phantoms of organs that are similar to the human body. The K-XRF HPGGe Cloverleaf detection system is able to detect Gd using a non-invasive method and can be used to answer the remaining questions. The research in the detection of Gd has advanced further and we are getting closer to the goal of reaching more knowledge about Gd retention and the safety of GBCAs for the sake of patients.

Bibliography

- [1] S. Bussi, A. Coppo, C. Botteron, V. Fraimbault, A. Fanizzi, E. De Laurentiis, S. Colombo Serra, M. Kirchin, F. Tedoldi, and F. Maisano. Differences in gadolinium retention after repeated injections of macrocyclic mr contrast agents to rats. *Journal of Magnetic Resonance Imaging*, 47(3):746–752, 2017.
- [2] S. Byun. Chapter 2, general properties of radiation detectors. *MED-PHYS 6R03: Radioisotopes and Radiation Methodology*, 2018.
- [3] C. Chumlea, S. Guo, C. Zeller, N. Reo, and R. Siervogel. Total body water data for white adults 18 to 64 years of age: The fels longitudinal study. *Kidney International*, 56(1):244–252, 1999.
- [4] J. Grafe. In vivo detection of gadolinium by prompt gamma neutron activation analysis: An investigation of the potential toxicity of gadolinium-based contrast agents used in mri. *Doctorate Paper*, pages 0–171, 2012.
- [5] J. L. Grafe, F. E. McNeill, S. H. Byun, D. R. Chettle, and M. D. Noseworthy. The feasibility of in vivo detection of gadolinium by prompt

- gamma neutron activation analysis following gadolinium-based contrast-enhanced mri. *Applied Radiation and Isotopes*, 69(1):105–111, 2011.
- [6] T. Grobner and F. C. Prischl. Gadolinium and nephrogenic systemic fibrosis. *Kidney International*, 72(3):260–264, 2007.
- [7] W. High, R. Ayers, J. Chandler, G. Zito, and S. Cowper. Gadolinium is detectable within the tissue of patients with nephrogenic systemic fibrosis. *Journal of the American Academy of Dermatology*, 56(1):21–26, 2007.
- [8] M. Khandaker. High purity germanium detector in gamma-ray spectrometry. *International Journal of Fundamental Physics Sciences*, 1(2):42–46, 2011.
- [9] G. F. Knoll. *Radiation Detection and Measurement*. John Wiley and Sons, Inc., Michigan, 1979.
- [10] P. Kuo, E. Kanal, A. Abu-Alfa, and S. Cowper. Gadolinium-based mr contrast agents and nephrogenic systemic fibrosis. *Radiology*, 242(3):647–649, 2007.
- [11] Michael F. L’Annunziata. *Radioactivity: Introduction and History, From the Quantum to Quarks*. Elsevier, Amsterdam, Netherlands, 2007.
- [12] S. Laurent, L. Vander Elst, F. Copoix, and R. Muller. Stability of mri paramagnetic contrast media: A proton relaxometric protocol for transmetallation assessment. *Investigative Radiology*, 36(2):115–122, 2001.

- [13] E. Ledneva, S. Karie, V. Launay-Vacher, N. Janus, and G. Deray. Renal safety of gadolinium-based contrast media in patients with chronic renal insufficiency. *Radiology*, 250(3):618–628, 2009.
- [14] M. Lord. In vivo detection of retained gadolinium in bone by x-ray fluorescence following administration of gadolinium-based contrast agents used in mri. *Doctorate Paper*, pages 0–138, 2019.
- [15] M. Lord, F. E. McNeill, J. L. Grafe, M. D. Noseworthy, and D. R. Chettle. Self-identified gadolinium toxicity: comparison of gadolinium in bone and urine to healthy gadolinium-based contrast agent exposed volunteers. *Physiological Measurement*, 39(11), 2018.
- [16] R. McDonald, J. McDonald, D. Dai, D. Schroeder, M. Jentoft, D. Murray, R. Kadirvel, L. Eckel, and D. Kallmes. Comparison of gadolinium concentrations within multiple rat organs after intravenous administration of linear versus macrocyclic gadolinium chelates. *Radiology*, 285(2):536–545, 2017.
- [17] N. Murata, L. Gonzalez-Cuyar, K. Murata, C. Fligner, R. Dills, D. Hippe, and K. Maravilla. Macrocyclic and other non-group 1 gadolinium contrast agents deposit low levels of gadolinium in brain and bone tissue: Preliminary results from 9 patients with normal renal function. *Investigative Radiology*, 51(7):447–453, 2016.

- [18] H. Nie, D. Chettle, L. Luo, and J. O'Meara. In vivo investigation of a new cd-109 gamma-ray induced k-xrf bone lead measurement system. *Physics in Medicine and Biology*, 51(2):351–360, 2006.
- [19] R. A. Pacer. Liquid scintillation and cherenkov counting characteristics of cd-109. *Journal of Radioanalytical and Nuclear Chemistry*, 155:129–140, 1991.
- [20] D. Pelowitz. *MCNP6 User's Manual*. U.S. Government, Los Alamos, 2013.
- [21] J. Ramalho, R. C. Semelka, M. Ramalho, R. H. Nunes, M. AlObaidy, and M. Castillo. Gadolinium-based contrast agent accumulation and toxicity: An update. *American Journal of Neuroradiology*, 37(7):1192–1198, 2016.
- [22] N. Ranger. The aapm/rsna physics tutorial for residents: Radiation detectors in nuclear medicine. *Imaging and Therapeutic Technology*, 19(2):481–502, 1999.
- [23] N. Schieda, J. I. Blaichman, A. F. Costa, R. Glikstein, C. Hurrel, M. James, P. J. Maralani, W. Shabana, A. Tang, A. and Tsampalieros, C. Pol, and S. Hiremath. Gadolinium - based contrast agents in kidney disease: Comprehensive review and clinical practice guideline issued by the canadian association of radiologists. *Canadian Association of Radiologists*, 69(2):136–150, 2018.

- [24] P. Scoullar, C. McLean, and R. Evans. Real time pulse pile-up recovery in a high throughput digital pulse processor. *AIP Conference Proceedings*, 1412(270), 2011.
- [25] A. Todd and D. R. Chettle. In vivo x-ray fluorescence of lead in bone: Review and current issues. *Environmental Health Perspectives*, 102(2):172–177, 1994.
- [26] G. White and M. Gibby, W. Tweedle. Comparison of gd(dtpa-bma) (omniscan) versus gd(hp-do 3a) (prohance) relative to gadolinium retention in human bone tissue by inductively coupled plasma mass spectroscopy. *Investigative Radiology*, 41(3):272–278, 2006.